

## X-ray hardening preceding the onset of SGR 1935+2154's radio pulsar phase

PEI WANG ,<sup>1,2</sup> JIAN LI ,<sup>3,4</sup> LONG JI ,<sup>5</sup> XIAN HOU ,<sup>6,7</sup> ERBIL GÜGERCINOĞLU,<sup>1,8</sup> DI LI ,<sup>9,1</sup>  
 DIEGO F. TORRES ,<sup>10,11,12</sup> YUTONG CHEN,<sup>1,13</sup> JIARUI NIU ,<sup>1,13</sup> WEI-WEI ZHU ,<sup>1,2</sup> BING ZHANG ,<sup>14</sup>  
 EN-WEI LIANG ,<sup>15</sup> LI ZHANG,<sup>16</sup> MINGYU GE ,<sup>17</sup> ZIGAO DAI ,<sup>3,4</sup> LIN LIN,<sup>2</sup> JINLIN HAN ,<sup>1</sup> YI FENG,<sup>18</sup> CHENHUI NIU,<sup>19</sup>  
 YONGKUN ZHANG ,<sup>1,13</sup> DEJIANG ZHOU ,<sup>1,13</sup> HENG XU,<sup>1,20</sup> CHUNFENG ZHANG ,<sup>1,20</sup> JINCHEN JIANG ,<sup>1,20</sup>  
 CHENCHEN MIAO ,<sup>18</sup> MAO YUAN ,<sup>21</sup> WEIYANG WANG,<sup>13,22</sup> DENGKE ZHOU ,<sup>18</sup> JIANHUA FANG ,<sup>18</sup> YOULING YUE ,<sup>1</sup>  
 YUNSHENG WU,<sup>23</sup> YABIAO WANG ,<sup>23</sup> CHENGJIE WANG,<sup>23</sup> ZHENYE GAN,<sup>23</sup> YUXI LI,<sup>23</sup> ZHONGYI SUN,<sup>23</sup> MINGMIN CHI,<sup>24</sup>  
 JUNSHUO ZHANG ,<sup>1,13</sup> JINHUANG CAO ,<sup>1,13</sup> WANJIN LU ,<sup>1,13</sup> AND YIDAN WANG ,<sup>1,13</sup>

<sup>1</sup>National Astronomical Observatories, Chinese Academy of Sciences, Beijing 100101, China

<sup>2</sup>Institute for Frontiers in Astronomy and Astrophysics, Beijing Normal University, Beijing 102206, China

<sup>3</sup>CAS Key Laboratory for Research in Galaxies and Cosmology, Department of Astronomy, University of Science and Technology of China, Hefei 230026, China

<sup>4</sup>School of Astronomy and Space Science, University of Science and Technology of China, Hefei 230026, China

<sup>5</sup>School of Physics and Astronomy, Sun Yat-Sen University, Zhuhai, 519082, China

<sup>6</sup>Yunnan Observatories, Chinese Academy of Sciences, Kunming 650216, China

<sup>7</sup>Key Laboratory for the Structure and Evolution of Celestial Objects, Chinese Academy of Sciences, Kunming 650216, China

<sup>8</sup>Istanbul University, Faculty of Science, Department of Astronomy and Space Sciences, Beyazit, 34119, Istanbul, Turkey

<sup>9</sup>Department of Astronomy, Tsinghua University, Beijing 100084, China

<sup>10</sup>Institute of Space Sciences (ICE, CSIC), Campus UAB, Carrer de Can Magrans, 08193, Barcelona, Spain

<sup>11</sup>Institut d'Estudis Espacials de Catalunya (IEEC), 08860 Castelldefels (Barcelona), Spain

<sup>12</sup>Institució Catalana de Recerca i Estudis Avançats (ICREA), E-08010, Barcelona, Spain

<sup>13</sup>University of Chinese Academy of Sciences, Beijing 100049, China

<sup>14</sup>Department of Physics and Astronomy, University of Nevada, Las Vegas, Las Vegas, NV 89154, USA

<sup>15</sup>Guangxi Key Laboratory for Relativistic Astrophysics, School of Physical Science and Technology, Guangxi University, Nanning 530004, China

<sup>16</sup>Department of Astronomy, Key Laboratory of Astroparticle Physics of Yunnan Province, Yunnan University, Kunming 650091, China

<sup>17</sup>Key Laboratory of Particle Astrophysics, Institute of High Energy Physics, Chinese Academy of Sciences, Beijing 100049, China

<sup>18</sup>Zhejiang Lab, Hangzhou, Zhejiang 311121, China

<sup>19</sup>Institute of Astrophysics, Central China Normal University, Wuhan 430079, China

<sup>20</sup>Department of Astronomy, Peking University, Beijing 100871, China

<sup>21</sup>National Space Science Center, Chinese Academy of Sciences, Beijing 101400, China

<sup>22</sup>Kavli institute for astronomy and astrophysics, Peking University; Beijing 100871, China

<sup>23</sup>Tencent YouTu Lab, Shanghai 201103, China

<sup>24</sup>Fudan University, Shanghai 200438, China

## ABSTRACT

Magnetars are neutron stars with extremely strong magnetic fields, frequently powering high-energy activity in X-rays. Pulsed radio emission following some X-ray outbursts have been detected (Camilo et al. 2006, 2007), albeit its physical origin is unclear. It has long been speculated that the origin of magnetars' radio signals is different from those from canonical pulsars, although convincing evidence is still lacking. Five months after magnetar SGR 1935+2154's X-ray outburst and its associated Fast Radio Burst (FRB) 20200428, a radio pulsar phase was discovered. Here we report the discovery of X-ray spectral hardening associated with the emergence of periodic radio pulsations from SGR 1935+2154 and a detailed analysis of the properties of the radio pulses. The observations suggest that radio emission originates from the outer magnetosphere of the magnetar, and the surface heating due

to the bombardment of inward-going particles from the radio emission region is responsible for the observed X-ray spectral hardening.

## 1. INTRODUCTION

SGR 1935+2154 is a Galactic magnetar discovered in 2014 by Swift-BAT (Stamatikos et al. 2014). Its spin period ( $\sim 3.24$  s) and spin-down rate imply a surface magnetic field of  $\sim 2.2 \times 10^{14}$  G (Israel et al. 2016). Its spatial consistency with a supernova remnant (SNR) G57.2+0.8 suggests an actual association, leading to a distance estimation of  $6.6 \pm 0.7$  kpc (Zhou et al. 2020). Since its discovery, SGR 1935+2154 has shown multiple outbursts: in 2015 February, 2016 May, 2019 November, 2020 April, 2021 September and 2022 October (Kozlova et al. 2016; Younes et al. 2017; Guver et al. 2021; Younes et al. 2022). Simultaneous with a hard X-ray burst (Li et al. 2021a; Mereghetti et al. 2020; Ridnaia et al. 2021; Tavani et al. 2021) on 28th April 2020, SGR 1935+2154 was observed to be associated with the first Galactic Fast Radio Burst (FRB) FRB 20200428 (CHIME/FRB Collaboration et al. 2020; Bochenek et al. 2020), thus providing the first confirmed link between FRBs and magnetars (Petroff et al. 2019; Cordes & Chatterjee 2019). This discovery promoted intense follow up observations with a number of radio telescopes. However, only a few radio bursts were detected and the radio pulsation from SGR 1935+2154 was missing (Zhang et al. 2020; Kirsten et al. 2021; Tang et al. 2021; Good & Chime/Frb Collaboration 2020; Bailes et al. 2021; Rea et al. 2012).

Among the  $\sim 30$  magnetars known (Olausen & Kaspi 2014)<sup>1</sup>, only five of them have shown radio pulsations (Swift J1818.0-1607, SGR 1745-2900, PSR J1622-4950, XTE J1810-197, 1E 1547.0-5408). A monitoring campaign of SGR 1935+2154 with the Five-hundred-meter Aperture Spherical radio Telescope (FAST) was carried out during the April 2020 outburst. A radio burst was detected on 30 April 2020 21:43:05 (coordinated universal time, UTC), two days after FRB 20200428. We then detected radio pulsations in 464 rotation cycles from SGR 1935+2154 with 563 pulses (Appendix Table 1), making it the sixth member of the rare radio magnetar population.

The primary objective of this study is to summarize the properties of the pulsed emission observed during the same epoch in October 2020, based on the radio detections made by FAST and the X-ray detections made by NICER and SWIFT. The second primary goal is to use this comprehensive analysis of combined radio and X-ray detections to address critical pieces of the astrophysical puzzle such as the following.

- What is the intrinsic correlation between the behaviour of the magnetar radio and X-ray radiation?
- Is there a different origin for magnetar radio emission and canonical pulsars?
- Can there be a unified origin story to understand these pulses and the first Galactic FRB?

The structure of this work is as follows: Section 2 describes the observations and data analysis procedures; Section 3 presents the pulse catalog and comprehensive radio pulsation analysis from our sample; Section 4 studies the bimodal behaviors of the X-ray hardness ratio, correlated with the activity level of radio emission; Section 5 discusses the radiation mechanism of the radio active period accompanied by the X-ray spectral hardening; Finally, our conclusions are summarized in Section 6.

## 2. OBSERVATION AND DATA REDUCTION

The depth and cadence of FAST monitoring allow us to do a detailed study of SGR 1935+2154. Part of the FAST data were also presented in Zhu et al. 2020, 2023, which presented a detailed study of the pulsar timing properties, but with completely different analysis. In this paper we focus on the unique X-ray spectral hardening in SGR 1935+2154, as it is the only confirmed radio-pulsation-related spectral change of magnetars on a months time scale.

### 2.1. FAST observation of SGR 1935+2154 and data reduction.

The FAST observation of SGR 1935+2154 was conducted for 45 hours mainly in the following two sessions: (i) from 15 April 2020 to 20 May 2020 (UTC); (ii) from 9 October 2020 to 7 November 2020 UTC, through the FRB key project of FAST. The distribution of radio pulse and temporal burst rates detected during the observation campaign of SGR J1935+2154 is shown in Figure 1. The central frequency was 1.25 GHz, spanning from 1.05 GHz to 1.45 GHz,

<sup>1</sup> <https://www.physics.mcgill.ca/~pulsar/magnetar/main>

including a 20 MHz band edge on each side. The average system temperature was 25 K. The recorded FAST data stream for pulsar observations is a time series of total power per frequency channel, stored in PSRFITS format (Hotan et al. 2004) from a ROACH-2 based backend, which produces 8-bit sampled data over 4k frequency channels at 49  $\mu$ s cadence. We searched for radio pulsations with either a dispersion signature or instrumental saturation in all FAST data collected during the observational campaign.

Four types of data processing were performed: I) folding the data according to the ephemerides derived from the X-ray data, II) dedicated single pulse search, III) baseline saturation search, and IV) Artificial Intelligence (AI) aided data filtering.

I. Exploit the X-ray ephemerides to fold for radio pulsed emission in FAST data: We analyzed the radio data of SGR 1935+2154 using the ephemerides derived from the X-ray data as well as the X-ray light curve during the time span covered by the FAST observation. We separately folded the FAST data from the whole observation as well as those dedicated time spans of detected single pulses.

II. Dedicated single pulse search: We created de-dispersed time series for each pseudo-pointing over a range of DMs from 200 - 450 pc cm $^{-3}$ , which should cover all the uncertainties in a semi-blind search. The step size between subsequent trial DMs ( $\Delta$ DM) was chosen such that over the entire band  $t(\Delta\text{DM}) = t_{\text{channel}}$ . This ensures that the maximum extra smearing caused by any trial DM deviating from the source DM by  $\Delta\text{DM}$  is less than the intra-channel smearing. We used the above dedicated search scheme to de-disperse the data. Then we used 14 grids of matching filters. The grids were distributed in logarithmic space from 0.1 ms to 30 ms. A zero-DM matched filter was applied to mitigate RFI in the blind search. All the possible candidate plots generated were then visually inspected. Most of the candidates were RFIs, and no pulsed radio emission with dispersive signature was detected with a S/N  $>7$ .

III. Saturation search: We understand that FAST would be saturated if the radio flux is as high as hundred-Jansky to mega-Jansky. We therefore also searched for saturation signals in the recorded data-set. We looked for the epoch in which 50% of channels satisfy one of the following conditions: 1) the channel is saturated (255 value in 8-bit channels), 2) the channel is zero-valued, 3) the RMS of the bandpass is less than 2. We did not detect any saturation lasting  $>0.5$  s, hence excluded any saturation associated during the observational campaign.

IV. AI aided data filtering: To further reduce the noise and interference in observation, we designed a learning-based filtering framework (Figure 2) for efficient data selection. In particular, for each observed data with arrival time  $t_a$  and trial DM, two types of input are extracted from the observation (1) A time-frequency array  $A_1$  cropped from original observation signal in the frequency window 1.05 GHz to 1.45 GHz, and time window starting from arrival time  $t_a$  and ending at  $t_a + \Delta t_1$ . The endurance  $\Delta t(s)$  can be estimated with the trial DM:

$$\Delta t_1 = 4148808.0 \times DM \times \left( \frac{1}{(1450/\text{MHz})^2} - \frac{1}{(1050/\text{MHz})^2} \right) / 1000 . \quad (1)$$

(2) A time-frequency array  $A_2$  cropped from de-dispersed observation with the same frequency window and the time window is centered at  $t_a$  and its duration  $\Delta t_2(s)$  is set as the time of 50 sampling bins.

Both arrays are preprocessed with min-max normalization before sending to AI model. We take ResNet-18 (He et al. 2016) as classification model to map the input array into a normalized confidence vector, indicating whether the input array belongs to a potential candidates. For each types of input, we train a classification model respectively. After training process, these two models are deployed to predict the corresponding confidence  $c_1, c_2$  for input  $A_1$  and  $A_2$  respectively. Finally, the confidence score is merged as

$$c = 0.08c_1 + 0.92c_2 . \quad (2)$$

If  $c > 0.1$ , the observation data will be sent to visual inspection, otherwise it will be discarded.

To train the classification network, we take the observation from FRB 20121102A (Li et al. 2021b) as training data, which are de-dispersed and visualized for manual labeling. If the visual observation shows strong visual feature and corresponds to the correct astronomical coordinates with a matching position error HPBW $\sim$ 3 arcmin (Jiang et al. 2020), it is labeled as 1 (positive) to denote this is a positive training sample, otherwise it is labeled as 0 (negative). To control the balance between positive and negative training samples, we adopt the active learning strategy of Selective-by-Distinctive-Margin (SDM) (Xie et al. 2022) by evaluating the distance from a data sample to different categorical clusters for data selection. When training classifier with  $A_2$ , the standard cross entropy is utilized as training loss. To train model with larger array of  $A_1$ , we take the multiple instance learning framework (Ilse et al. 2018) to train the classifier on multiple subarrays of  $A_1$ . We then calibrated the noise level of the baseline with noise CAL injection

and then measured the intensity values of the detected significant pulse profiles, giving the flux measurement and uncertainties for the detected pulses.

## 2.2. NICER and Swift data analysis

To study the outburst evolution, we analysed all NICER observations on SGR 1935+2154 recorded along 2020. The first NICER observation (obs ID 3020560101, on April 28) is within the burst storm of the source (Younes et al. 2020), thus it was excluded from the study of outburst evolution, which is mainly focused on the persistent emission. A bright dust-scattering halo was detected around SGR 1935+2154 in the Neil Gehrels Swift Observatory (Swift-XRT) observation on April 27. Shortly it decayed to nearly background level on April 28 (Mereghetti et al. 2020). Thus, excluding the first NICER observation from our analysis also eliminated the possible contamination from the dust-scattering halo. NICER observational data was processed following the NICER Data Analysis Guide<sup>2</sup>. NICERDAS version 8c incorporated in the HEASOFT version 6.29c was used in the NICER data analysis to process observation data from level 1. The source and background spectra were produced using nibackgen3C50 (see the NICER Data Analysis Guide in footnote)<sup>3</sup>, adopting the 2020 background model. NICER response (RMF) and effective area (ARF) files were produced using NICERrmf and NICERarf.

To increase statistics, several nearby spectra from individual observations were combined to have at least 5000 events. Then the spectra were grouped to have at least 50 counts per energy channel using GRPPHA. The hydrogen column density is fixed at  $2.4 \times 10^{22} \text{ cm}^{-2}$  following previous studies (Younes et al. 2020), which is also consistent with (Coti Zelati et al. 2018). Considering the large absorption and reduced NICER sensitivity at high energies, we limit our spectral analysis of SGR 1935+2154 in the range of 1-5 keV. All spectra could be well fitted using an absorbed blackbody plus powerlaw model, adopting the Tubingen-Boulder model (tbabs) for interstellar absorption with the abundances adopted in this study (Wilms et al. 2000). Because of the fitting energy range and statistics, the photon index was fixed at 1.2 (Borghese et al. 2020; Göğüş et al. 2020). The NICER observations are listed in Table 2.

Swift-XRT has monitored the 2020 X-ray outburst of SGR 1935+2154. To avoid the burst storm and focus on the persistent emission of the source, we excluded Swift observations before April 29. During the monitoring campaign, Swift-XRT has been working in both Photon Counting (PC) and Window Timing (WT) mode. For a lower background level, only data in PC mode were used in this paper. The Swift observational data was processed following the dedicated pipeline<sup>4</sup>. We selected PC data with event grades 0–12. A circular region centered on SGR 1935+2154 with a radius of 30 pixels (1pixel=2.36 arcsec) were adopted to extract the spectrum of source. Background spectrum were extracted from source-free region with a same size. Spectra were combined for a higher statistics and analyzed in the range of 1–10 keV, adopting a similar method as in NICER data. The Swift-XRT observations are listed in Table 3.

## 3. COMPREHENSIVE RADIO PULSATION ANALYSIS

We measured the peak flux density, equivalent pulse width and fluence etc. for each pulse (see Appendix Table 1 for the full catalog). The timeline of the pulse fluence during the FAST observation campaign, combined with reported measurements of upper limits at various radio instruments/frequencies (Bailes et al. 2021) are shown in the upper panel of Figure 3. The average fluence is  $0.03 \pm 0.01 \text{ Jy ms}$ , which is 7–8 orders of magnitude lower than that of FRB 20200428. The pulse rate peaked at  $139 \text{ hr}^{-1}$  on 10 October (MJD 59132) and at  $137 \text{ hr}^{-1}$  on 11 October (MJD 59133), which means that the fraction of rotation periods with pulse detection is  $\sim 10\%$  of the total number of rotation periods during the corresponding observation time (see Figure 1). The pulse rate then precipitously dropped by an order of magnitude.

Radio pulses from SGR 1935+2154 have shown unique time-frequency properties, among which broad & narrow-band emission and an interesting sub-pulse time–frequency upward- or downward-drifting morphology. We identify three observed archetypes of pulse morphology in SGR 1935+2154 (Figure 4, upper panel a, b, c). Narrow-band and frequency drifting emissions were seen in FRB morphology (Pleunis et al. 2021) (e.g. FRB 20121102A, Figure 4, panel d, e, f), but rarely observed in normal pulsars, and never detected in magnetars before SGR 1935+2154. The drifting rate of the so-called downward frequency drifting morphology in the dynamic spectrum was defined by Hessels et al. (Hessels et al. 2019).

<sup>2</sup> [https://heasarc.gsfc.nasa.gov/docs/NICER/data\\_analysis/NICER\\_analysis\\_guide.html](https://heasarc.gsfc.nasa.gov/docs/NICER/data_analysis/NICER_analysis_guide.html)

<sup>3</sup> [https://heasarc.gsfc.nasa.gov/docs/nicer/data\\_analysis/nicer\\_analysis\\_guide.html](https://heasarc.gsfc.nasa.gov/docs/nicer/data_analysis/nicer_analysis_guide.html)

<sup>4</sup> <https://swift.gsfc.nasa.gov/analysis/>

### I) DM VARIATION

To quantify the specific morphological characteristics of the pulsation, the optimum dispersion measure (DM) should be determined. We utilized the incoherent dispersion technique using the single-pulse-search tool in PRESTO (Ransom 2001). De-dispersed pulse profiles were created for each DM trial between 300 to 350 pc cm<sup>-3</sup> with a step size of 0.05 pc cm<sup>-3</sup> to maximize the ‘local contrast’ of the dedispersed pulse profile. Gaussians (multiple when necessary) were fitted to the structure function of the profiles  $I(DM, t)$ . The derivative of each Gaussian was then squared. For multiple components, the square of the derivative of the pulse profiles was summed. The optimized DM<sub>obs</sub> was then determined through the maximization of the area under the squared derivative profiles, thus maximizing the structures in the frequency integrated burst profile:

$$DM_{obs} = \arg \max_{DM} \left\{ \sum_t \left( \frac{dI(DM, t)}{dt} \right)^2 \right\} \quad (3)$$

the FWHM of the fitted DM is taken as the uncertainty. The optimal DM of the pulses is finally constrained to be  $332.7 \pm 0.1$  pc cm<sup>-3</sup> between MJD 59131 and MJD 59167.

The DM distribution of these pulses exhibits no significant time-evolutionary feature. In order to test the reliability of the no-evolutionary trend of DM, we divided the DM measurements into two time-epochs according to the dates of the event and generated mock DM values in each bin, based on the mean and the standard deviation of the measured DMs in the respective time bins. The null hypothesis was then tested based on the generated DMs under the assumption that DM does not change over time. For each set of generated DMs, a slope was fitted. Based on 20,000 trials, the central value of the slope distributions is zero with a  $\sigma$  of  $\sim 0.004$  pc cm<sup>-3</sup> yr<sup>-1</sup> for both time-epochs. The rapid fluctuations in DM values between pulses can be attributed either to the low flux density that does not allow for a good fit to the pulse profiles, or to external causes such as turbulent motion of clumps or filaments in the surrounding pulsar wind environment.

### II) ENERGY DISTRIBUTION

The pulse rate versus pulse energy distribution of SGR 1935+2154 shows a broad bump (Figure 5). We test the hypothesis that the energy distribution can be described by a power-law function  $N(E) = N_1 E^{-\alpha_E}$  in a certain energy range  $E_i \leq E \leq E_f$ :

$$N_1 = \frac{N_{ev}(1 - \alpha_E)}{E_f^{1-\alpha_E} - E_i^{1-\alpha_E}}, \quad (4)$$

where  $N_1$  is the normalization constant, and  $N_{ev}$  is the total number of pulses included. This definition is only valid for the index  $\alpha_E \neq 1$ , while the integral takes the form of  $\propto \ln(E)$  for  $\alpha_E = 1$ . The energy function is consistent with a power law with  $\alpha_E = 3.3 \pm 0.2$  and a central energy around  $4.8 \times 10^{27}$  erg for the energy range  $E \geq 2.5 \times 10^{27}$  erg with a coefficient of determination  $R^2 = 0.928$ .

This distribution is time dependent and shows a bimodality along time. There are days with significantly higher pulse rate averages, although the averaged pulse energy variations is small. The high energy pulses are more concentrated before MJD 59140 (Figure 6). There is no significant correlation between the averaged pulse energy with its standard deviation for each day and the pulsed event rate. The fewer events after that epoch may signify that the bimodality is due to time-dependent lensing, but more plausibly it might be an analog of “mode changes” commonly seen in long period radio pulsars where pulse components change their relative amplitudes and occurrence rates. Further observations can distinguish between these possibilities.

We measured the peak flux density, pulse width and fluence, then calculated the isotropic equivalent energy of each pulse based on the latest distance estimation to SGR 1935+2154 ( $6.6 \pm 0.7$  kpc (Zhou et al. 2020)) at 1.25 GHz. The derived pulse energies span more than one order of magnitude, from  $5 \times 10^{26}$  erg to  $\sim 10^{28}$  erg. The normalized cumulative distribution of the pulse rate for SGR 1935+2154 (hereafter defined as “survival rate” in Figure 5) can be well fitted by a single threshold power-law function with index of  $3.3 \pm 0.2$  after considering the instrumental detection completeness bias. The index of SGR 1935+2154 is similar to known pulsars or pulsar giant pulses (GPs) with a steep slope, and is different from that of FRBs, which on average is more shallow. We compared the pulse fluence cumulative distributions of classical pulsars (Bilous et al. 2022), GPs (Bera & Chengalur 2019), repeating FRBs (FRB 20121102A (Li et al. 2021b), FRB 20190520B (Niu et al. 2022) and FRB 20201124A (Zhang et al. 2022)) and SGR 1935+2154. The fluences are normalized both by the average and standard deviation of fluence in logarithmic space (Figure 5).

The distribution of SGR 1935+2154 is clearly separate from the Crab pulsar GPs and PSR B0950+08, but tend to follow the trend of FRB 20190520B and is likely consistent with FRB 20201124A in the lower end of fluence.

### III) MORPHOLOGY

The pulsed radio emission from magnetars is usually characterized by a flat radio spectral index ( $S_\nu \propto \nu^{0.5}$ ) and large variabilities both in flux density and pulse profile (Camilo et al. 2006; Kramer et al. 2007).

We described the frequency band-pass of pulses with signal to noise ratio ( $S/N \geq 10$ ) using the phenomenologically power-parabola function (Thulasiram & Lin 2021)  $I = \kappa(\frac{\nu}{\nu_0})^{\alpha+\beta \log(\frac{\nu}{\nu_0})}$ , where  $\nu$  is a frequency value between 1.0 and 1.5 GHz of FAST L-band receiver,  $I$  is the amplitude (arbitrary units) at a given frequency,  $\alpha$ ,  $\beta$ , and  $\kappa$  are three of the free parameters and  $\nu_0 = 1.25$  GHz is the reference frequency. A higher  $\beta$  indicates narrower frequency band emission. The fitting function would degenerate to a power-law function with  $\beta \sim 0$ . We estimated the fitting uncertainties through the standard error propagation to avoid over fitting. The distributions of the morphological fitting parameters  $\alpha$  and  $\beta$  are shown in the panel (a) of Figure 7. The distribution of  $\beta$  against  $\alpha$  clearly separates the narrow-band and broad-band pulses. Narrow-band pulses (higher  $\beta$ ) tend to have a steeper spectrum (higher  $|\alpha|$ ) than broad-band ones. A power-law (PL) distribution ( $\beta = A|\alpha|^\gamma$ ) is fitted to the two branches ( $\alpha \leq 0$  and  $\alpha \geq 0$ ) (panel a2) with respective index of  $\gamma_l$  and  $\gamma_r$ . The best-fit  $\gamma_l$  and  $\gamma_r$  are the same ( $1.1 \pm 0.02$ ) and the residuals have no obvious structure (Figure 7, panel a3). Furthermore, the distribution of  $\kappa$  against  $\beta$  and  $\alpha$  (7, panel b and c) suggests that  $\kappa$  is also a discriminating parameter for narrow-band pulses. Narrow-band pulses (higher  $\beta$  and  $|\alpha|$ ) are less bright (lower  $\kappa$ ) than broad-band ones. The pulses show a similarly observed archetypes of FRB morphology (Pleunis et al. 2021), and have an apparent difference from representative young pulsars.

The radio pulsations' frequency drifting rate of SGR 1935+2154 is  $\dot{\nu} \sim 10$  GHz per second. With the observation frequency  $\nu_{\text{obs}} = 1.45$  GHz, it would suggest a radio emission location, following equation 1 in Yang et al. 2020:

$$R_{\text{radio}} \sim \frac{c\nu_{\text{obs}}}{\dot{\nu}_{\text{drift}}} = 4.35 \times 10^9 \text{ cm}, \quad (5)$$

which is within the light cylinder radius  $R_{LC} = c/2\pi\nu = 15.5 \times 10^9$  cm but far away from the magnetar surface ( $R_{\text{magnetar}} \sim 10^6$  cm). This suggests that the radio emission of SGR 1935+2154 is most likely originated from the closed field lines region in the outer magnetosphere through the formation of a current loop originated from the twisting magnetospheric field line (hereafter referred to as "j-bundle"), rather than the polar cap region as in canonical radio pulsars.

### IV) TIME-DOMAIN ANALYSIS

To quantify the specific time-domain characteristics of pulses, we take the pulse profile above the detection threshold as a separate pulse. To be conservative, we take the detection threshold using the 3-sigma noise level of the baseline due to the complicated effect on the actual sensitivity, e.g. the bandwidth limited structure of the pulses and radio frequency interference (RFI) events. On the other hand, we tried to differentiate the pulses by referring to the morphological clustering characteristics of the pulses in the dynamic spectrum. Figure 8 shows pulse width  $W_{\text{eq}}$  against fluence distribution. The equivalent width  $W_{\text{eq}}$  is defined as the width of a rectangular pulse that has the same area as the detected pulse, and the height of the peak flux density is denoted as  $S_{\text{peak}}$ . In our sample, several pulses might be described with multiple components in a single pulsation, if there is "bridge" emission (higher than  $5\sigma$ ) between pulses for the pulses with a complex time-frequency structure. This results in some pulses having overestimated equivalent widths. The computed  $W_{\text{eq}}$  range from 0.9 ms to  $\sim 40$  ms, consistent with a log-normal distribution centered around  $\sim 6$  ms. This is consistent with the known statistical properties of repeating FRBs, and RRAT population (Li et al. 2021b; Maciesiak & Gil 2011).

We also studied the statistical property of the waiting time distribution. The waiting time between two adjacent detected pulsations is  $\delta t = t_{i+1} - t_i$ , where  $t_{i+1}$  and  $t_i$  are the corresponding bary-centred arrival times for the  $(i+1)$ th and  $(i)$ th bursts. All waiting times were calculated for pulses within the same session to avoid long gaps of  $\sim 24$  hr. Figure 9 shows the occurrence rates (green region) as a function of waiting times as well as its cumulative distribution (solid black line) of the waiting time. The cumulative distribution of the pulse rate can be well fitted from Monte Carlo Markov Chain (MCMC) method using a single threshold power-law function with index of  $1.96 \pm 0.01$  (solid red line in Figure 9). We found similar occurrence frequency distributions of waiting time for FRBs (Gourdji et al. 2019; Wang et al. 2021; Aggarwal et al. 2021), which also supports the temporal tight correlation between the SGR 1935+2154 pulsations and repeating FRBs.

The Lomb–Scargle periodogram method is widely used to identify periodicities in data that are not uniformly sampled. We here apply this method to the nulling of rotation periods to determine whether there is a possible period. If the active phase of nulling does have a period, folding the time intervals of nulling according to amplitude-modulated periodicities would show clustering in burst phase, suggesting a modulation pattern compatible with a rotating beam-carousel model. Periodograms of nulling from SGR 1935+2154 for periods ranging from 2 to 100 are shown in Figure 10. No periodicity of the nulling time was found in the power spectrum. Folding with that period does not show any concentration in pulse phase. In addition, we design an experiment in order to test whether the periodicity of Nulling has a possible pulse energy dependence. We divide all the detected pulses into two groups: the full pulse and the bright pulse with  $S/N \geq 15$  are subjected to the periodic search separately, and the power spectra of the two groups are compared. The test results show that neither group reflects any sign of periodicity in nulling, and that lack of periodicity for the pulsation nulling intervals is independent of the grouping of pulse energy sizes. All observing sessions fall in the pulsation active phase of SGR 1935+2154, thus the pulsation nulling intervals also did not reveal any underlying modulation periodicity.

#### 4. BIMODAL BEHAVIORS OF THE X-RAY HARDNESS RATIO, CORRELATED WITH THE ACTIVITY LEVEL OF RADIO EMISSION

We carried out a detailed comprehensive pulse analysis on energy, duration and waiting time for SGR 1935+2154, which shows an apparent difference from representative young pulsars. Previously detected five other magnetars (Swift J1818.0-1607, SGR 1745-2900, PSR J1622-4950, XTE J1810-197, 1E 1547.0-5408), the radio pulsations of which are usually detected shortly after their respective X-ray outbursts. (Camilo et al. 2007; Halpern et al. 2008). At some point, the radio pulsations may disappear without related activities in other wavelengths (e.g. in X-rays), to rise again in other outbursts. The delays between radio pulsations and the onset of X-ray outbursts range from as short as  $\sim 35$  hours (Swift J1818.0-1607 (Karuppusamy et al. 2020)) to  $\sim 18$  days (XTE J1810-197 (Caleb et al. 2022; Lyne et al. 2018)). For SGR 1745-2900 and 1E 1547.0-5408, the delay times are  $\sim 5$  days (Rea et al. 2013) and  $\sim 3$  days &  $\sim 16$  days (Bernardini et al. 2011; Camilo et al. 2009; Lower et al. 2023), respectively. For PSR J1622-4950, the radio bursts were first detected in 2009, and again in 2017, years after the prior closest X-ray observation, during which, however, no X-ray burst was detected, thus rendered the delay time uncertain (Levin et al. 2010; Anderson et al. 2012; Camilo et al. 2018). Out of all five magnetars aforementioned, the X-ray spectral hardening associated with radio pulsation was only observed in SGR 1745-2900 (Kaspi et al. 2014; 5 days delay). However, Kaspi et al. argued that such behavior could originate from a different source within the NuSTAR PSF, due to its proximity to the Galactic center. Thus, the X-ray spectral hardening in SGR J1935+2154 is unique: it is the only confirmed radio-pulsation-related spectral change, and has a time scale of months.

SGR 1935+2154 has however manifested a different behavior. Radio observations on SGR 1935+2154 are shown in Figure 3, together with the X-ray outburst evolution observed by NICER and Swift-XRT. Its regular radio pulsation was not activated in line with the X-ray outburst, but delayed for several months. The radio active episode of SGR 1935+2154 (green solid lines in Figure 3, lower panels) lasts  $\sim 50$  days at most, by far the shortest among radio magnetars. During the radio active episode, a significant spectral hardening was detected while the X-ray activity level decayed. The X-ray flux hardness ratio (2.5-5 keV/1.5-2.5 keV) observed by combining NICER and SWIFT (Figure 3) underwent a sudden drop around MJD 59140, and then experienced an apparent increase until MJD 59150, reaching the hardest spectrum during the X-ray outburst decay. Dramatic X-ray spectral changes during magnetar outbursts are common, generally starting from a rapid initial hardening and then entering a slow softening as the flux decays to quiescence<sup>5</sup> (Kaspi & Beloborodov 2017; Coti Zelati et al. 2018).

In SGR 1935+2154, we discovered the first confirmed significant spectral hardening while the magnetar outburst decays and with associated radio activity. The Hardness-Intensity Diagram (HID) is a model independent way for tracking the spectral evolution. The panel a of Figure 11 shows the HID for the SGR 1935+2154's outburst in 2020. The X-ray data during the radio active period (red (NICER) & pink (Swift) points) take a different branch from the other outburst decaying period (blue (NICER) & black (Swift) points). Red and pink data points could be well fitted with a linear function  $y = ax + b$ , yielding fitting parameters  $a=1.54\pm 0.09$ ,  $b=0.63\pm 0.07$  and a reduced  $\chi^2$  of 1.25 (d.o.f=10). We calculated the cumulative  $\chi^2$  of blue and black data points against the linear fitting (Figure 11, panel b) quoted above. It shows a significant increasing trend, indicating that the X-ray data during the radio active

<sup>5</sup> SGR 1745-2900 has shown spectral hardening during X-ray decay, but could be due to a different source appearing within the NuSTAR PSF considering its proximity to the Galactic center (Kaspi et al. 2014).

and quiet period took a different spectral evolution, perhaps suggesting they may originate from distinct emission processes.

We propose a Crustquake-Outburst-Transient scenario to explain the results reported in this paper. All the observed phenomena, including the frequency drifts, the emergence of radio pulsations several months after the onset of the X-ray outburst, and its accompanied spectral hardening in X-rays shown in Figure 3, could be explained in a self-consistent framework based on energy release from twisted field lines within the magnetar’s magnetosphere

## 5. RADIATION MECHANISM OF THE RADIO ACTIVE PERIOD ACCOMPANIED BY THE X-RAY SPECTRAL HARDENING

The origin of the magnetar radio emission is still unclear. It might arise from the open field region in the magnetosphere above the polar cap, similar to the pulsed radio emission of canonical radio pulsars (Ruderman & Sutherland 1975; Philippov & Kramer 2022), or from a j-bundle, which is thicker in size and more energetic than the electron acceleration region above the polar cap (Istomin & Sobyanin 2007; Beloborodov 2013).

The occurrence of FRB 20200428 after the onset of SGR 1935+2154’s burst forest in X-rays, its delayed radio active period, and accompanying X-ray spectral hardening behaviour shown in Figure 3, can be qualitatively understood within the standard scenario of magnetar outbursts (Thompson & Duncan 2001). A sudden energy release near the magnetar surface accompanies a crust cracking quake. Part of the energy dissipated heats up the magnetar surface and forms a trapped fireball of electron/positron pairs ( $e^\pm$ ) and soft X-rays in the closed field line region of the magnetosphere near the surface. The high outburst energy with  $T \sim 80$  keV (estimated from the cutoff energy in the spectrum of FRB 20200428 (Ioka 2020)) may lead to the formation of an optically thick  $e^\pm$  outflow surrounding the fireball, which pushes FRB photons along open field lines in the magnetosphere. Since the fireball was formed after the crustquake powering the outburst, there should be a finite time delay between the outburst and the FRB, as observed for SGR 1935+2154.

The magnetic field inside a magnetar is twisted. After a crustquake, part of the magnetic energy and twist are carried over to the closed field lines. The twisting of magnetospheric field lines leads to the formation of the so-called current carrying j-bundle. Coherent radio curvature emission is generated by the charge fluctuations in the corresponding bundle. Since the magnetic field lines are twisting slowly after the crustquake, the pulsed radio emission appears with a delay compared to the outburst in X-rays. In addition, the particle return currents with Lorentz factors  $\gamma \gtrsim 100$  bombard the magnetar surface and heat it up (González-Caniulef et al. 2019; Salmi et al. 2020). Particle bombardment onto the magnetar from the charge fluctuating bundle produces a thermally emitting hot spot on the cooling surface. This may explain the observed spectral hardening around MJD 59150. The active period of coherent radio emission depends on the time-scale of untwisting of magnetospheric field lines (Beloborodov 2009):

$$\begin{aligned} t_{\text{ev}} &= \frac{BR^2\Delta\psi_0}{cV} \\ &\approx 40 \left( \frac{B}{4.4 \times 10^{14}\text{G}} \right) \left( \frac{R}{15\text{km}} \right)^2 \left( \frac{\Delta\psi_0}{0.1} \right) \left( \frac{V}{10^9\text{volts}} \right)^{-1} \text{d} \end{aligned} \quad (6)$$

Here  $B$  is the dipolar component of the magnetic field on the polar cap,  $R$  is the neutron star radius,  $\Delta\psi_0$  is the twist angle,  $c$  is the speed of light and  $V$  is the voltage difference. With typical parameters of SGR 1935+2154, Equation 6 yields a radio active period of  $\sim 40$  days, which fits the FAST detection well. The delayed appearance of pulsed radio emission, its active period, and the accompanied X-ray spectral hardening support the scenario of crustquake-induced j-bundle current formation.

The precise radiation mechanism producing FRBs within the magnetar framework has not been fully understood yet. Two classes of models can be identified according to where the FRB is generated. The so-called “far-away” models, according to which FRBs are generated well outside the magnetar light cylinder, rely on a relativistic outflow that drives a shock into the surrounding circumstellar medium through magnetar winds or flares, and a short duration radio burst is produced by plasma maser and synchrotron radiation processes (Lyubarsky 2014; Metzger et al. 2019; Plotnikov & Sironi 2019; Beloborodov 2020). The predicted shock-powered X-ray fluence is close to the observed FRB 20200428 (Margalit et al. 2020), which indicates that part of the X-ray burst may come from shock emission. These models, however, face difficulties in explaining the double peak structure of FRB 20200428, as their narrow separation by 30 ms between the two peaks seems to be contradictory with the required larger length-scales for the synchrotron radiation from maser emission region (Margalit et al. 2020). Also, the implied plasma frequency cannot be reconciled with the observed luminosity (Lu et al. 2020).

By contrast, for models that propose FRBs generated inside the magnetar magnetospheres, several coherent radiation processes are feasible. In the model of Ref. (Kumar & Bošnjak 2020), FRBs are as a result of the coherent curvature radiation of  $e^\pm$  clumps accelerated in the induced electric field, parallel to the magnetic field, at the charge starvation radius that are generated by Alfvén waves launched into the magnetosphere after a crustquake. The coincidence of hard X-ray spikes and radio peaks can be understood within this framework. This model predicts that the FRB is produced at a distance  $R_{\text{FRB}} \sim 20(\delta B_{10}/\lambda_{\perp 4})^{6/11} R_{\text{NS}}$  with  $R_{\text{NS}}$  being neutron star radius,  $\delta B_{10}$  being the amplitude of the Alfvén wave disturbance at the magnetar surface in units of  $10^{10}$  G and  $\lambda_{\perp 4}$  being the wavelength perpendicular to the magnetic field in units of  $10^4$  cm. Then, the most likely location of the double peaked FRB 20200428 is two separated open magnetic field lines at a few tens of neutron star radii from the surface. The charged clump will radiate within an emission cone of opening angle  $\theta \sim \gamma^{-1}$  with  $\gamma$  being the Lorentz factor gained by charged particles during acceleration along the curved field line (Kumar et al. 2017) and the pair separation maintains narrow spectrum (Yang et al. 2020). The observed downward frequency drifting with time is a natural consequence of coherent curvature radiation by clumps of pairs in the outer magnetosphere through two stream instability (Wang et al. 2019).

For SGR 1935+2154 radio pulsations' frequency drifting rate  $\dot{\nu}_{\text{drift}} \sim 10 \text{ GHz s}^{-1}$  and observation frequency  $\nu_{\text{obs}} = 1.45 \text{ GHz}$ , Equation 5 yields a location  $\sim 4.35 \times 10^9 \text{ cm}$ , which is within the light cylinder radius  $R_{\text{LC}} = c/2\pi\nu = 15.5 \times 10^9 \text{ cm}$ . Therefore, FRB 20200428 can be produced at the open magnetic field region above the magnetic poles by  $e^\pm$  pairs whereas the radio pulsations of SGR 1935+2154 are generated by similar coherent curvature radiation at closed field lines region in the outer magnetosphere by the formation of a j-bundle.

Seismic energy released into the magnetosphere following crustal failure ignites FRB 20200428 right after the breaking event and the azimuthal motion of the broken platelet slowly twists the magnetic field lines, giving rise to transient pulsed radio emission through fluctuations in the magnetospheric charged particle density. For both processes a crustquake on the magnetar surface is the underlying trigger mechanism. Thus, crustquakes not only supply the right amount of energy budget powering the frequent X-ray outbursts on SGR 1935+2154 but also lead to FRBs and transient pulsed radio emission.

## 6. CONCLUSION

We discover delayed radio pulsations associated an X-ray spectral hardening in SGR J1935+2154, i.e. it is the only confirmed radio-pulsation-related spectral change and has a time scale of months, based on the radio detections made by FAST and the X-ray detections made by NICER & SWIFT. In this work, the observations suggest that radio emission originates from the outer magnetosphere of the magnetar, and the surface heating due to the bombardment of inward going particles from the radio emission region is responsible for the observed X-ray spectral hardening. The Crustquake-Outburst-Transient model based on observations in this work provides a unified origin story for these pulses and the first Galactic FRB.

Through a comprehensive analysis of 563 radio pulses in October 2020 and the contemporaneous X-ray behavior of the magnetar SGR 1935+2154, we found (i) an X-ray spectral hardening that correlates with active radio emission, while the X-ray flux faded; (ii) narrow-band as well as frequency-drifting radio pulses, distinct from normal pulsars; (iii) a radio emission location of in the outer magnetosphere consistent with the measured frequency drifting rate. All of the above could be explained by the energy released from twisted field lines within the magnetar's magnetosphere, providing evidence that the magnetar radio emission mechanism differs from that of canonical radio pulsars.

<sup>1</sup> This work is supported by National Natural Science Foundation of China (NSFC) Programs No. 11988101, No. 11725313, No. 11690024, No. 12273038, No. 12373051, No. 12041303, No. U1731238, No. 12173103; by CAS International Partnership Program No. 114-A11KYSB20160008; by CAS Strategic Priority Research Program No. XDB23000000; and the National Key R&D Program of China (No. 2017YFA0402600); and the National SKA Program of China No. 2020SKA0120200. D.L. is a New Cornerstone investigator. P.W. acknowledges support from the National Natural Science Foundation of China (NSFC) Programs No.11988101, 12041303, the CAS Youth Interdisciplinary Team, the Youth Innovation Promotion Association CAS (id. 2021055), and the Cultivation Project for FAST Scientific Payoff and Research Achievement of CAMS-CAS. D.F.T. acknowledges support from the Spanish grants PID2021-124581OB-I00, 2021SGR00426, CEX2020-001058-M and EU PRTR-C17.I1. This work made use of data from FAST, a Chinese national mega-science facility built and operated by the National Astronomical Observatories, Chinese Academy of Sciences.

*Facilities:* FAST, NICER, Swift

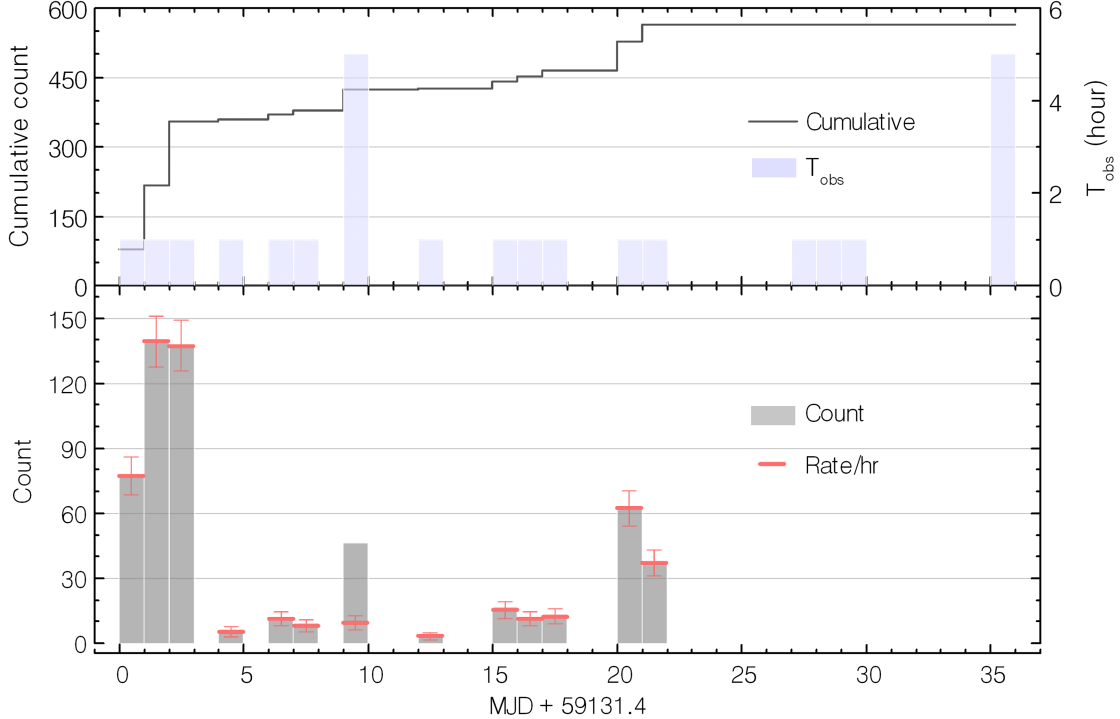


**Figure 1.** Detected radio pulse and temporal burst rate distributions of SGR J1935+2154 during the observation campaign. Upper panel: the duration of each observation session (blue bar, right axis) and the cumulative count distribution of the pulses (solid line, left axis). Bottom panel: the count (grey bar) and rate (red line) of the radio pulses detected.

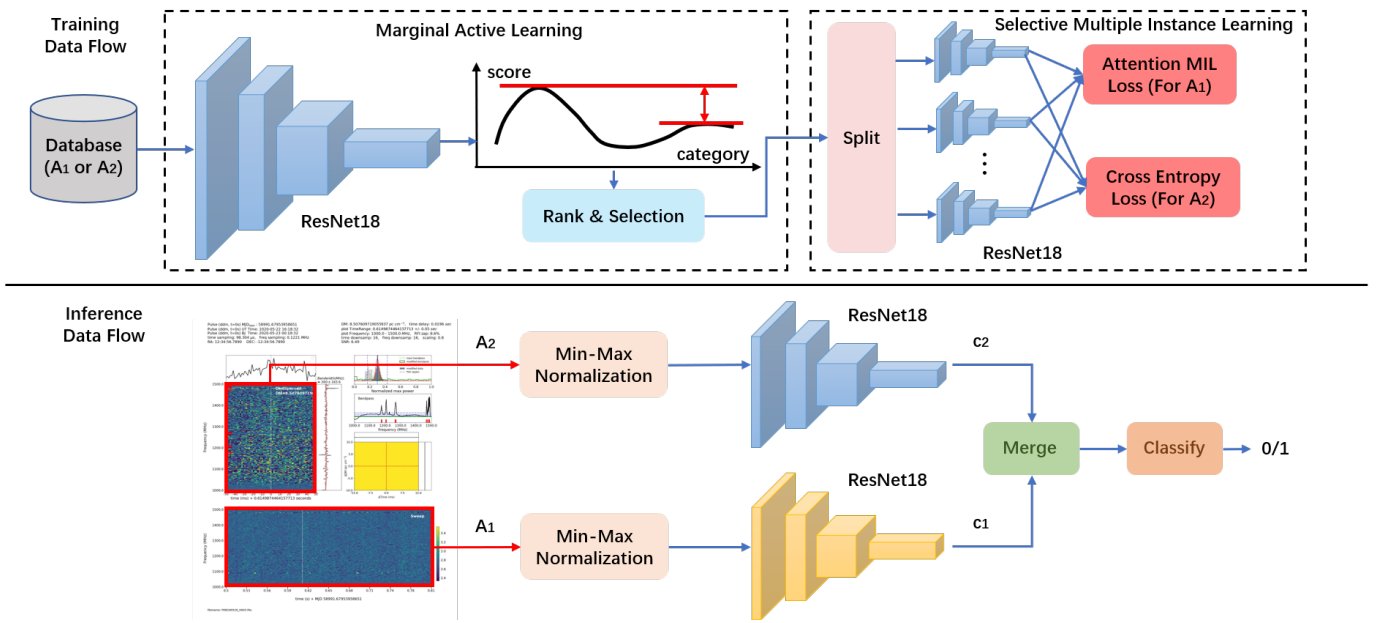


**Figure 2.** Data flow of AI aided observation data filter. Upper panel: the training data flow to guide the Deep Neural Network (DNN) to fit the joint distribution of positive and negative training samples from FRB 20121102A (Li et al. 2021b). Bottom panel: the inference data flow when taking well trained classifier for online data filtering.

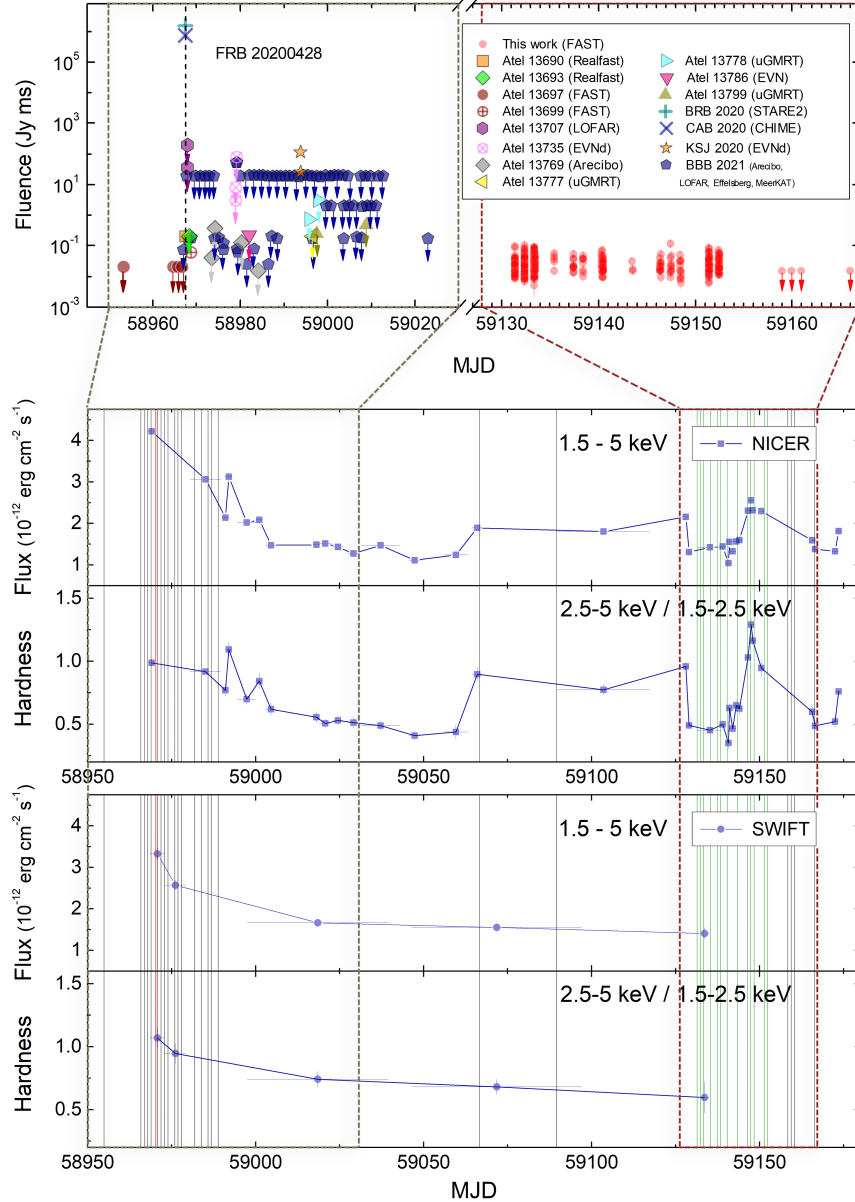


**Figure 3.** Timeline of detected radio pulses and X-ray light curves of SGR J1935+2154 during the observation campaign. (Upper panel) Temporal pulse fluences or upper limits at various radio instruments/frequencies. The red dots represent all 563 pulses detected by FAST in 464 rotation periods from MJD 59131 to 59167, the downward arrows indicate each upper-limit measurement. (Bottom panel) From top to bottom: SGR 1935+2154 NICER/SWIFT-XRT light curves in 1.5-5 keV and hardness ratio (2.5-5 keV/1.5-2.5 keV) . The solid lines indicate FAST observations with radio flare (red), no radio pulsation (black) and with radio pulsation (green).

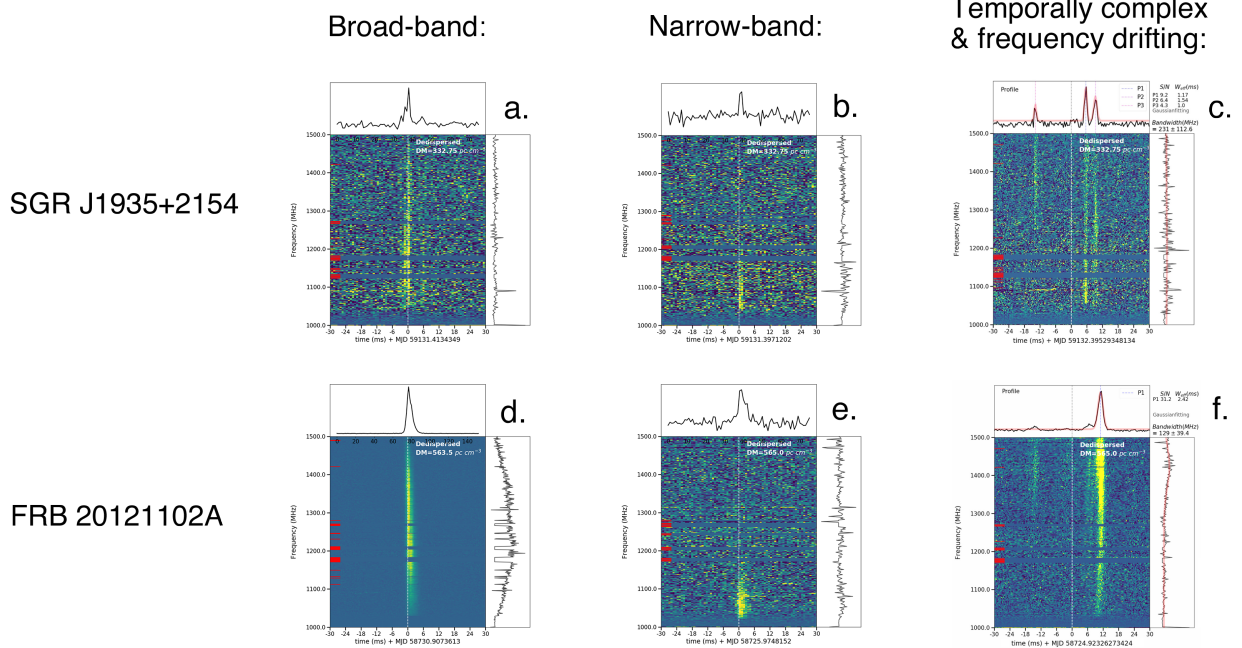


**Figure 4.** Three archetypes of pulse morphology in the time-frequency waterfall plots. Rows from left to right: Broad-, narrow-band, and temporary complex/frequency drifting dedispersed dynamic spectra of the radio pulse morphology of SGR 1935+2154 as detected by FAST on Oct. 2020, compared to repeating FRB 20121102A (also with FAST, between 29 Aug. and 4 Sep. 2019). The archetype spectra of SGR 1935+2154 show an interesting morphological similarity with repeating FRB. The band-averaged time series and time-averaged spectra are shown on the top and right sides of panel (c) and (f), respectively, with the Gaussian-fitted models overplotted by red-solid lines.

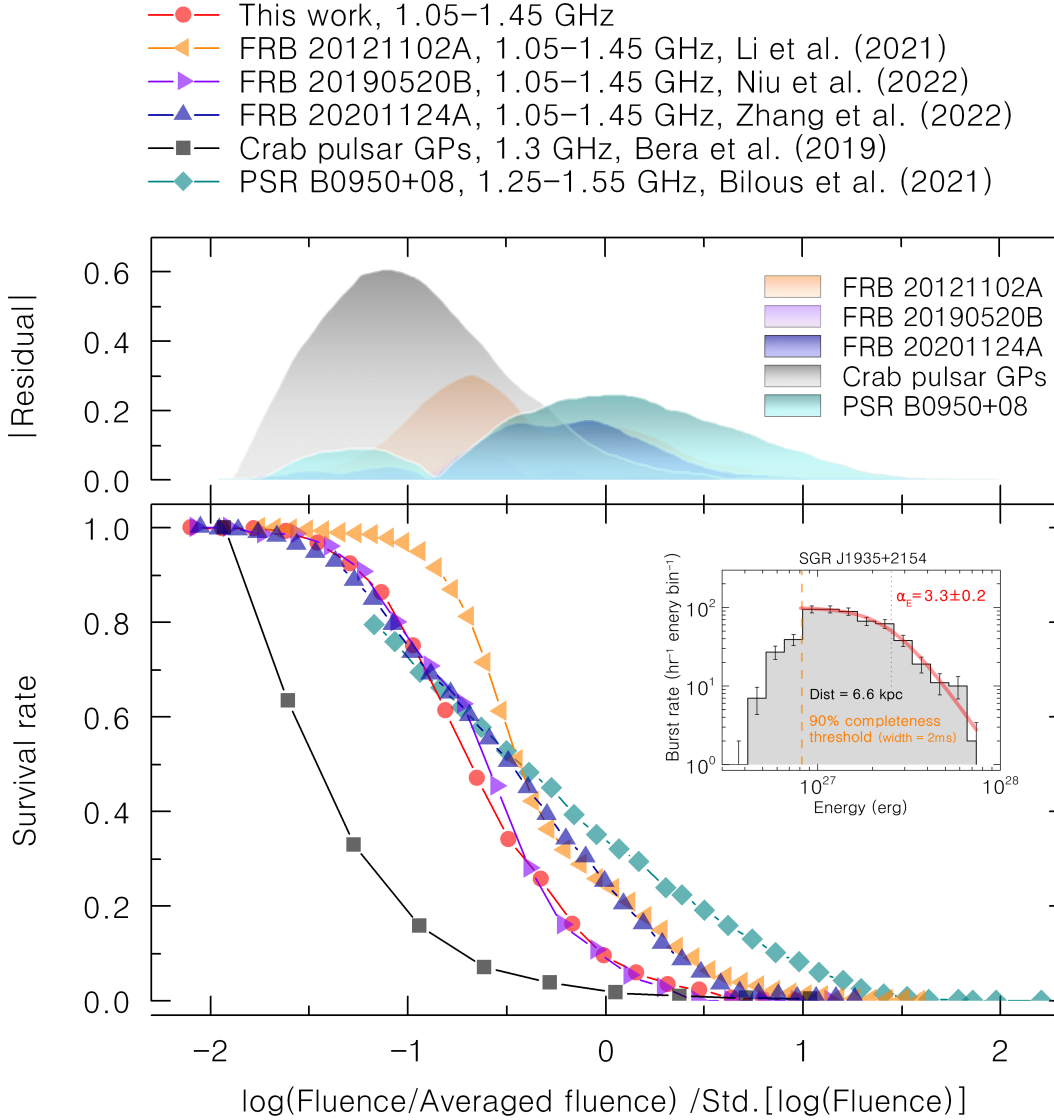


**Figure 5.** Comparison of the single-pulse fluence cumulative distribution for classical pulsars, pulsar giant pulses (GPs), FRBs and SGR 1935+2154. The collection of fluences are normalized both by their averaged fluences and standard deviation, respectively. The subplot is the pulse rate distribution of the isotropic equivalent energy at 1.25 GHz for SGR 1935+2154 pulses. A single power-law fit for pulses above a certain threshold  $E \geq 2.5 \times 10^{27}$  erg is shown in red solid line, and the 90% detection completeness threshold is shown with the yellow dashed line.

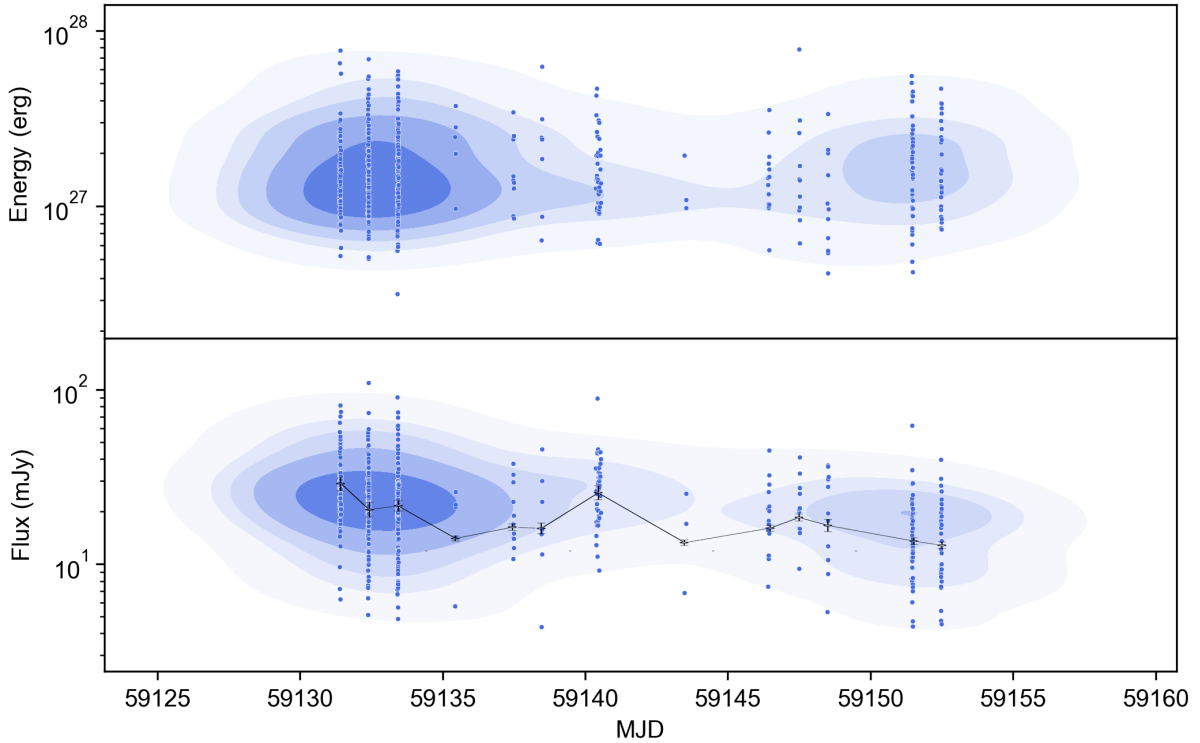


**Figure 6.** The 2D kernel density estimation (KDE) of the pulses detected from SGR 1935+2154. Upper panel: the isotropic energy KDE (blue contours) assuming a distance of 6.6 kpc. Lower panel: the flux KDE (blue contours) and the average value for each observation session (black points).

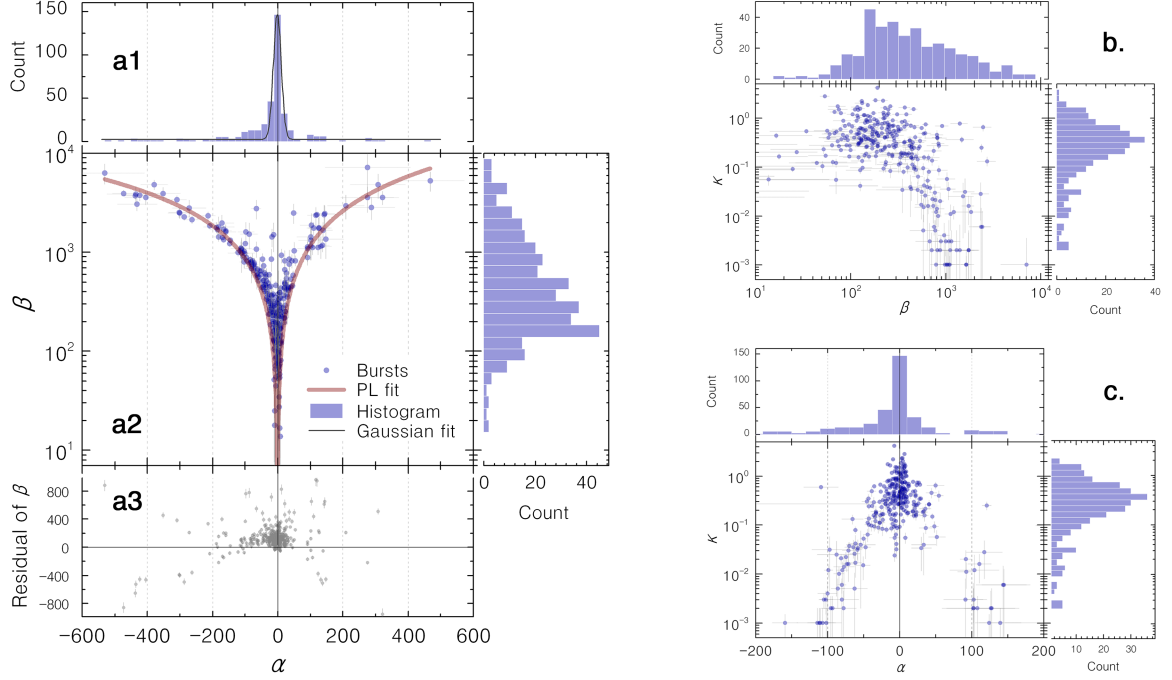


**Figure 7.** The distributions of the morphological fitting parameters  $\alpha$ ,  $\beta$  and  $\kappa$ . In each of the lower left plots of each panel, the points represent pulses with  $S/N > 10$  from the set of 563 pulses detected. The error-bars are calculated at the 68% confidence level. In each panel, the top plot is the histogram of the x-axis data, and the right plot is the histogram of the y-axis data. Panel (a):  $\alpha$  vs  $\beta$ , a clear separation of the narrow- and broad-band populations suggests  $\beta$  is a discriminating parameter between them. Two-component PL distribution is separately fitted in red solid line (panel a2), and the fitting residual is in the bottom panel a3). Panel (b) shows  $\kappa$  vs  $\beta$ , and Panel (c) indicates  $\kappa$  vs  $\alpha$ .

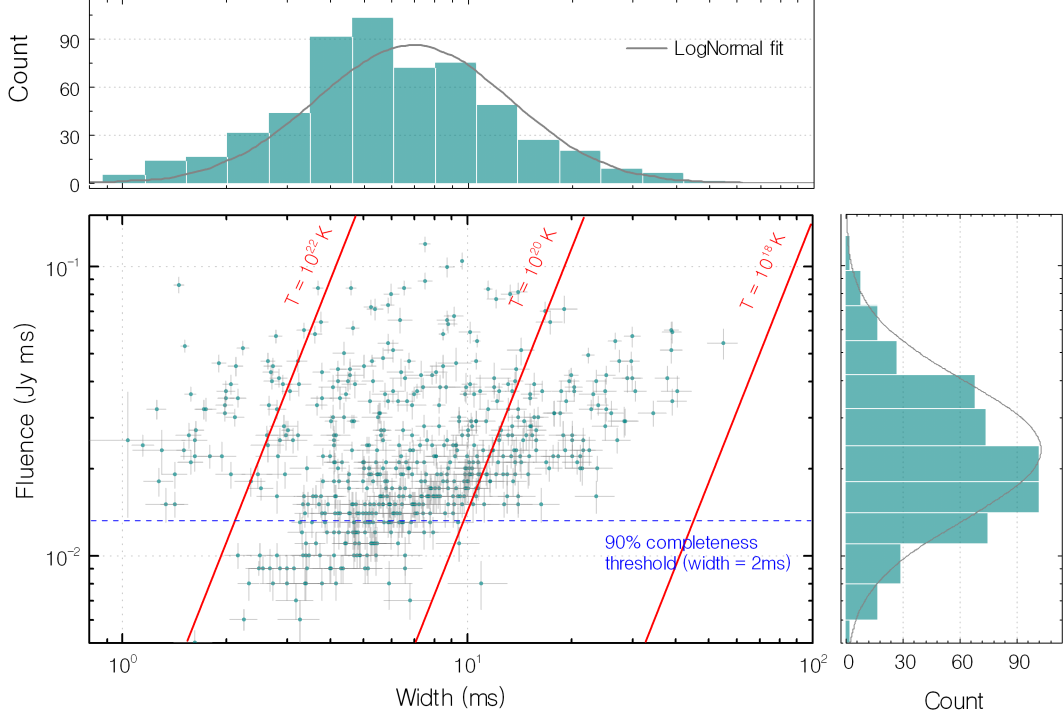


**Figure 8.** The fluence and equivalent pulse width distributions at 1.25 GHz for SGR 1935+2154. The dots indicate all of the 563 detected pulses, the red solid lines represent the equivalent brightness temperatures, and the horizontal blue dashed line is the simulated 90% detection completeness threshold. In the upper panel, an overall log-normal (LN) distribution is fitted in grey line.

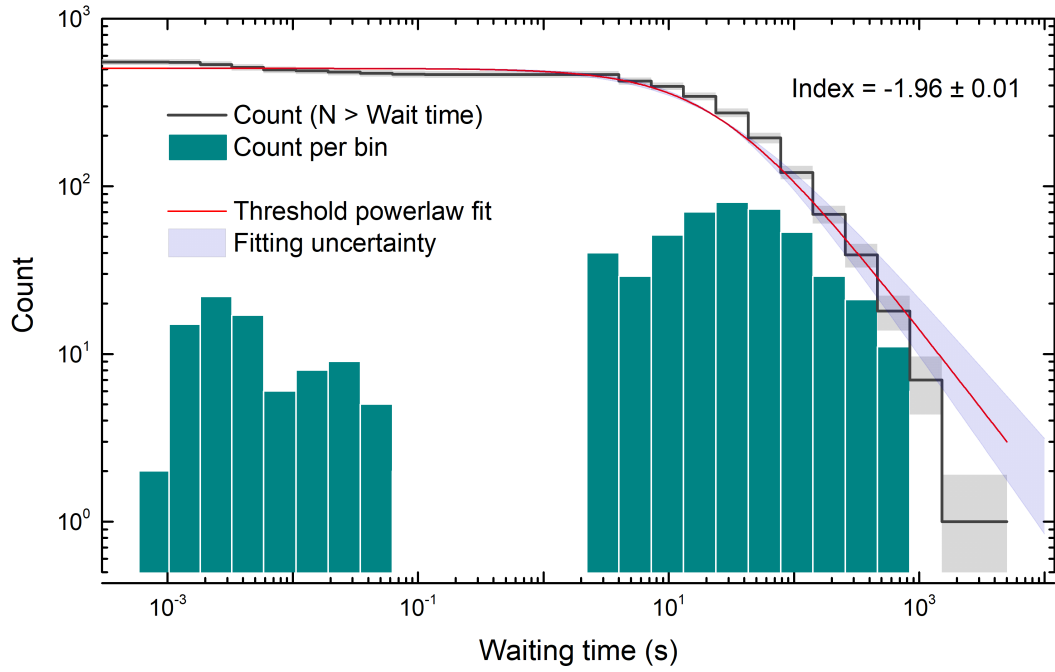


**Figure 9.** Waiting-time frequency distribution. We give the differential (green region) and cumulative (solid black line) distribution of waiting-time, respectively. Solid red line represents an overall fit for the cumulative distribution of the pulse rate using a single threshold power-law function with index of  $1.96 \pm 0.01$ , while the shaded region indicates fitting uncertainty.

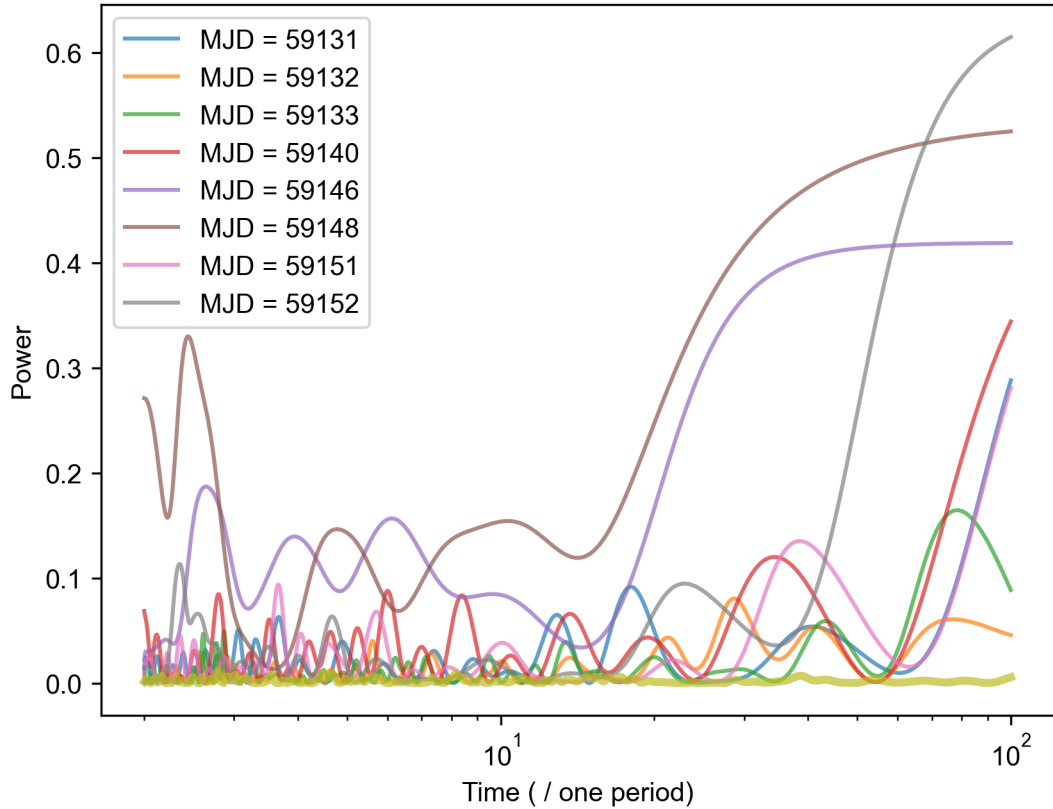


**Figure 10.** Lomb-Scargle periodograms of nulling periods for SGR 1935+2154. Nulling period has been searched from 2 to 100 rotational periods, and no distinct concentration has been found in all of the pulse active phases.

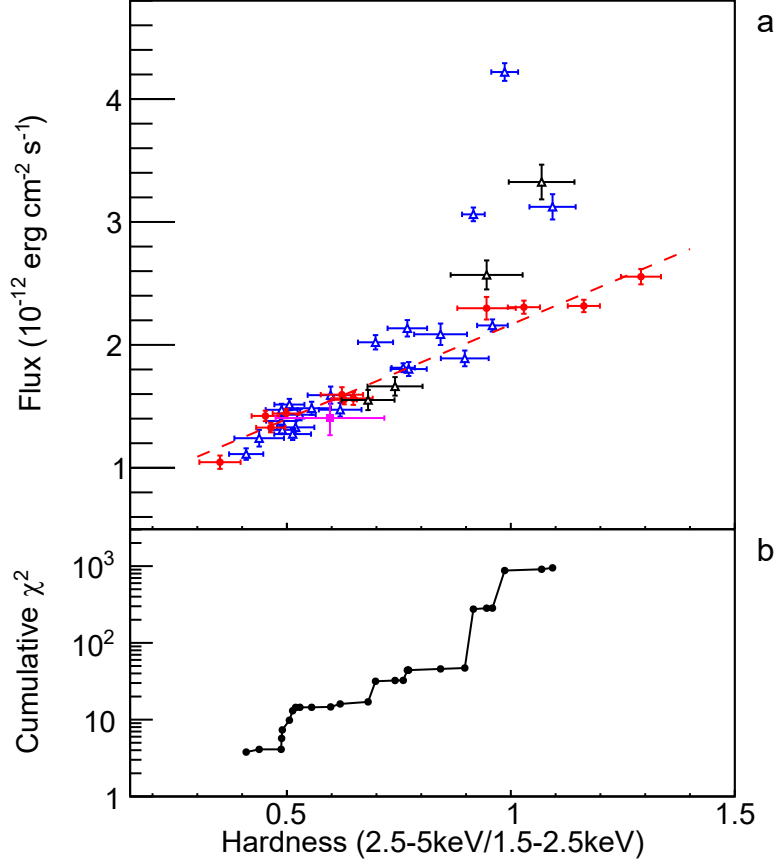


**Figure 11.** Panel a: Hardness-Intensity Diagram of SGR 1935+2154. The flux is in the 1.5-5 keV band. The red and pink data points are derived from NICER and Swift-XRT observations when SGR 1935+2154 shows radio pulsations, while the blue and black data points represent the rest of the NICER and Swift-XRT observations. The dashed red line represents the linear fitting of the observations when SGR 1935+2154 shows radio pulsations (red and pink data) points. Panel b: cumulative  $\chi^2$  for observations when SGR 1935+2154 shows no radio pulsations against the linear fitting, showing a trend of deviation.

## APPENDIX

## A. APPENDIX INFORMATION

**Table 1. The properties of 563 bursts of SGR 1935+2154 measured with FAST**

Pulse ID	Rot. period	$T_{start}/T_{obs}$	Pulse ToA <sup>a)</sup>	Width	Peak flux	Fluence	Energy	Cntrl freq.	Bandwidth <sup>b)</sup>	DM <sup>c)</sup>
		(MJD/hour)	(MJD)	(ms)	(mJy)	(Jy ms)	( $\times 10^{27}$ erg)	(MHz)	(MHz)	(pc cm <sup>-3</sup> )
1	1	59131.3843958 /	1.059131.384713925	4.2 (2)	47.1 (26)	0.020 (2)	1.3 (1)	1277	69	332.5 (5)
2		/	59131.384713944	4.1 (4)	24.6 (14)	0.010 (2)	0.6 (1)	1236	86	332.5 (5)
3	2	/	59131.386969843	4.6 (4)	30.0 (17)	0.014 (2)	0.9 (1)	1230	154	333.0 (9)
4	3	/	59131.387270595	23.7 (15)	17.3 (10)	0.040 (4)	2.6 (4)	1256	253	333.3 (3)
5	4	/	59131.388134811	4.9 (4)	29.0 (16)	0.014 (2)	0.9 (1)			332.2 (5)
6		/	59131.388134844	14.0 (17)	11.8 (7)	0.016 (2)	1.1 (2)			332.2 (5)
7	5	/	59131.388736181	3.5 (2)	43.2 (24)	0.015 (2)	1.0 (1)			332.8 (2)
8	6	/	59131.389299918	4.3 (2)	48.3 (27)	0.021 (2)	1.3 (1)			332.7 (1)
9	7	/	59131.389638961	14.5 (11)	17.8 (10)	0.025 (2)	1.7 (3)	1316	169	331.3 (3)
10		/	59131.389638989	12.1 (11)	16.0 (9)	0.019 (2)	1.2 (2)	1318	160	331.3 (3)
11	8	/	59131.389901356	8.6 (5)	28.8 (16)	0.024 (2)	1.6 (2)	1357	97	333.3 (3)
12		/	59131.389901434	12.0 (7)	32.4 (18)	0.038 (3)	2.5 (3)			333.3 (3)
13		/	59131.389901607	5.1 (3)	33.7 (19)	0.017 (2)	1.1 (2)			333.3 (3)
14	9	/	59131.390051526	5.9 (4)	27.4 (15)	0.016 (2)	1.0 (1)	1240	345	332.4 (3)
15	10	/	59131.390465440	4.1 (1)	65.0 (36)	0.026 (2)	1.7 (2)	1088	59	332.7 (3)
16	11	/	59131.390503145	25.1 (19)	14.8 (8)	0.037 (4)	2.4 (4)	1096	48	331.9 (3)
17	12	/	59131.391781648	6.1 (6)	24.2 (13)	0.014 (2)	0.9 (2)	1168	81	332.8 (8)
18	13	/	59131.392270009	2.0 (1)	23.8 (13)	0.037 (3)	2.4 (4)			332.8 (1)
19	14	/	59131.393247383	7.8 (6)	21.5 (12)	0.016 (2)	1.1 (2)	1115	148	331.9 (4)
20	15	/	59131.393660636	3.3 (2)	37.1 (21)	0.012 (2)	0.8 (1)			332.1 (4)
21	16	/	59131.393923638	14.2 (13)	15.6 (9)	0.022 (2)	1.4 (3)	1164	142	332.8 (2)
22	17	/	59131.395728087	8.7 (4)	14.5 (8)	0.099 (8)	6.5 (9)	1133	39	332.4 (1)
23		/	59131.395728251	8.3 (7)	20.0 (11)	0.016 (2)	1.1 (2)	1133	39	332.4 (1)
24	18	/	59131.397833033	8.1 (6)	27.4 (15)	0.022 (2)	1.4 (2)	1107	125	332.7 (0)
25		/	59131.397833078	7.8 (7)	22.1 (12)	0.017 (2)	1.1 (2)			332.7 (0)
26		/	59131.397833214	5.5 (2)	57.3 (32)	0.031 (2)	2.0 (2)	1117	186	332.7 (1)
27	19	/	59131.398096292	4.1 (2)	44.6 (25)	0.018 (2)	1.2 (1)	1469	315	332.1 (6)
28	20	/	59131.398923336	7.0 (4)	33.6 (19)	0.023 (2)	1.5 (2)	1090	98	332.6 (1)
29	21	/	59131.402006687	9.2 (9)	17.0 (9)	0.015 (2)	1.0 (2)	1178	275	332.2 (2)
30	22	/	59131.402043610	9.4 (4)	32.0 (18)	0.030 (2)	1.9 (2)			332.6 (1)
31	23	/	59131.402306870	8.0 (8)	20.7 (11)	0.016 (2)	1.1 (2)	1113	71	332.8 (2)
32	24	/	59131.402908218	5.4 (4)	26.0 (14)	0.014 (2)	0.9 (1)			332.2 (2)
33	25	/	59131.403245990	4.1 (3)	29.4 (16)	0.012 (1)	0.8 (1)	1162	162	331.6 (5)
34	26	/	59131.404035959	6.7 (4)	30.2 (17)	0.020 (2)	1.3 (2)	1250	192	332.4 (6)
35	27	/	59131.404148320	5.6 (2)	48.0 (27)	0.027 (2)	1.7 (2)			332.0 (3)
36	28	/	59131.404937998	9.9 (9)	17.8 (10)	0.017 (2)	1.1 (2)	1102	72	332.5 (7)
37	29	/	59131.404975811	3.3 (2)	46.5 (26)	0.015 (2)	1.0 (1)			332.4 (7)
38	30	/	59131.405126033	6.4 (5)	25.2 (14)	0.016 (2)	1.0 (2)			332.4 (3)
39	31	/	59131.405576826	8.0 (7)	20.7 (11)	0.016 (2)	1.1 (2)	1174	274	332.1 (5)
40	32	/	59131.407794496	7.9 (9)	15.4 (9)	0.012 (2)	0.8 (2)	1000	110	333.3 (8)

**Table 1.** The properties of 563 bursts of SGR 1935+2154 measured with FAST

Pulse <i>ID</i>	Rot. period	T <sub>start</sub> / T <sub>obs</sub> (MJD/hour)	Pulse ToA <sup>a)</sup> (MJD)	Width (ms)	Peak flux (mJy)	Fluence (Jy ms)	Energy ( $\times 10^{27}$ erg)	Cntrl freq. (MHz)	Bandwidth <sup>b)</sup> (MHz)	DM <sup>c)</sup> (pc cm <sup>-3</sup> )
41		/	59131.407794521	6.0 (4)	25.2 (14)	0.015 (2)	1.0 (1)	1000	110	333.3 (8)
42	33	/	59131.407982048	4.6 (2)	49.5 (27)	0.023 (2)	1.5 (2)	1109	143	332.5 (1)
43	34	/	59131.408057846	4.4 (4)	21.4 (12)	0.009 (1)	0.6 (1)	1111	120	332.2 (4)
44		/	59131.408057906	3.0 (2)	11.0 (6)	0.026 (3)	1.7 (3)	1365	72	332.2 (4)
45	35	/	59131.408208078	9.3 (9)	19.2 (11)	0.017 (2)	1.1 (2)	1207	243	332.5 (6)
46	36	/	59131.408433868	4.4 (1)	81.2 (45)	0.036 (2)	2.3 (2)			332.7 (0)
47	37	/	59131.408659420	5.0 (3)	41.2 (23)	0.020 (2)	1.3 (2)	1297	310	332.5 (7)
48	38	/	59131.409862451	3.8 (2)	37.6 (21)	0.014 (2)	0.9 (1)			333.4 (7)
49	39	/	59131.410839505	3.4 (3)	23.8 (13)	0.008 (1)	0.5 (1)			333.8 (3)
50	40	/	59131.411215774	11.5 (6)	28.3 (16)	0.032 (2)	2.1 (3)			332.3 (7)
51	41	/	59131.412117474	4.7 (4)	25.2 (14)	0.012 (2)	0.8 (1)	1416	101	333.0 (3)
52		/	59131.412117482	4.1 (2)	39.1 (22)	0.016 (2)	1.0 (1)	1498	186	333.0 (3)
53	42	/	59131.413809816	6.9 (5)	27.3 (15)	0.019 (2)	1.2 (2)	1148	193	332.8 (9)
54	43	/	59131.414072514	10.3 (5)	27.8 (15)	0.028 (2)	1.8 (2)	1189	261	332.7 (1)
55	44	/	59131.414147828	4.1 (2)	51.7 (29)	0.021 (2)	1.4 (2)	1166	241	332.8 (3)
56	45	/	59131.414523783	7.6 (4)	33.4 (18)	0.025 (2)	1.6 (2)			332.7 (1)
57	46	/	59131.414899235	13.8 (6)	29.6 (16)	0.040 (3)	2.6 (3)	1098	48	332.6 (2)
58	47	/	59131.415236927	7.5 (3)	51.9 (29)	0.038 (3)	2.5 (3)	1193	230	332.5 (1)
59		/	59131.415236942	6.8 (2)	70.4 (39)	0.047 (3)	3.1 (4)	1160	192	332.4 (1)
60		/	59131.415237001	7.4 (8)	19.4 (11)	0.014 (2)	0.9 (2)	1096	49	332.5 (1)
61	48	/	59131.415387498	10.0 (10)	17.3 (10)	0.017 (2)	1.1 (2)	1100	82	332.7 (3)
62		/	59131.415387514	4.1 (2)	52.5 (29)	0.021 (2)	1.4 (2)	1105	108	332.7 (3)
63	49	/	59131.415425151	6.0 (5)	22.0 (12)	0.013 (2)	0.8 (1)	1322	74	332.4 (7)
64	50	/	59131.415876537	9.6 (6)	27.0 (15)	0.026 (2)	1.7 (2)	1123	169	333.1 (3)
65	51	/	59131.415989129	5.1 (6)	20.0 (11)	0.010 (2)	0.7 (1)	1359	88	332.9 (3)
66		/	59131.415989144	7.4 (7)	21.6 (12)	0.016 (2)	1.0 (2)	1359	88	332.9 (3)
67	52	/	59131.416515425	7.9 (2)	54.0 (30)	0.042 (3)	2.7 (3)	1000	153	332.7 (1)
68	53	/	59131.416703781	5.1 (4)	27.0 (15)	0.014 (2)	0.9 (1)			332.5 (8)
69	54	/	59131.418282987	5.0 (4)	24.0 (13)	0.012 (2)	0.8 (1)	1156	216	333.0 (3)
70	55	/	59131.420086855	6.3 (6)	21.0 (12)	0.013 (2)	0.9 (2)			332.8 (8)
71	56	/	59131.420501064	7.9 (5)	30.7 (17)	0.024 (2)	1.6 (2)	1139	166	332.7 (1)
72	57	/	59131.421966429	1.5 (0)	75.0 (42)	0.086 (6)	5.6 (7)	1117	74	332.7 (0)
73	58	/	59131.422041568	1.3 (0)	31.9 (18)	0.032 (2)	2.1 (3)	1359	169	333.0 (2)
74	59	/	59131.422191877	4.0 (4)	22.1 (12)	0.009 (1)	0.6 (1)	1109	91	332.9 (0)
75		/	59131.422191891	5.4 (5)	20.6 (12)	0.011 (2)	0.7 (1)	1100	106	332.9 (0)
76	60	/	59131.422342451	1.6 (1)	19.3 (11)	0.025 (2)	1.6 (3)			332.9 (8)
77	61	/	59131.422642629	1.2 (0)	27.0 (15)	0.024 (2)	1.6 (2)	1119	106	332.8 (1)
78	62	59132.3676593 / 1.059132.368043558	23.2 (20)	16.0 (10)	0.036 (4)	2.4 (5)	1084	80	334.2 (2)	
79	63	/	59132.368306749	29.0 (26)	14.5 (9)	0.041 (4)	2.7 (5)			332.9 (1)
80	64	/	59132.368494300	13.5 (10)	21.2 (13)	0.028 (2)	1.8 (3)	1148	257	332.5 (6)
81	65	/	59132.368606988	5.2 (5)	25.9 (16)	0.013 (2)	0.9 (1)	1164	78	332.3 (1)
82	66	/	59132.369058275	4.5 (4)	31.0 (19)	0.014 (2)	0.9 (2)	1322	184	332.4 (2)
83	67	/	59132.369734879	3.8 (1)	21.5 (13)	0.064 (5)	4.2 (6)	1178	198	332.3 (5)
84	68	/	59132.369810173	5.7 (2)	47.4 (29)	0.027 (2)	1.7 (2)			332.9 (2)
85	69	/	59132.371689825	7.4 (7)	20.1 (12)	0.015 (2)	1.0 (2)	1344	357	332.8 (8)
86		/	59132.371689855	5.2 (4)	27.4 (17)	0.014 (2)	0.9 (1)	1344	357	332.6 (8)

**Table 1.** The properties of 563 bursts of SGR 1935+2154 measured with FAST

Pulse ID	Rot. period	T <sub>start</sub> / T <sub>obs</sub>	Pulse ToA <sup>a)</sup>	Width	Peak flux	Fluence	Energy	Cntrl freq.	Bandwidth <sup>b)</sup>	DM <sup>c)</sup>
		(MJD/hour)	(MJD)	(ms)	(mJy)	(Jy ms)	( $\times 10^{27}$ erg)	(MHz)	(MHz)	(pc cm <sup>-3</sup> )
87	70	/	59132.372441536	5.6 (4)	28.1 (17)	0.016 (2)	1.0 (2)	1338	230	333.0 (8)
88	71	/	59132.373757859	3.3 (3)	31.3 (19)	0.010 (1)	0.7 (1)	1174	109	332.7 (9)
89	72	/	59132.374885327	5.7 (5)	26.4 (16)	0.015 (2)	1.0 (2)	1137	231	333.2 (8)
90	73	/	59132.375449016	1.8 (1)	23.2 (14)	0.032 (3)	2.1 (3)	1102	100	332.8 (2)
91	74	/	59132.377290865	6.3 (2)	54.3 (33)	0.034 (2)	2.2 (3)	1201	168	332.6 (1)
92	75	/	59132.37815497030.1	19.3 (16)	0.057 (4)	3.7 (6)				332.5 (2)
93	76	/	59132.378343808	5.6 (2)	56.8 (34)	0.031 (2)	2.0 (3)	1324	163	332.4 (1)
94	77	/	59132.37845607139.2	15.3 (25)	0.059 (5)	3.8 (6)	1383	51	332.2 (2)	
95	78	/	59132.378643479	2.0 (1)	14.6 (9)	0.022 (2)	1.5 (3)	1154	220	332.2 (5)
96	79	/	59132.378982140	14.6 (9)	20.0 (12)	0.029 (2)	1.9 (3)	1357	323	332.6 (5)
97	80	/	59132.379960092	5.8 (9)	9.2 (6)	0.021 (4)	1.4 (4)			332.4 (7)
98	81	/	59132.380185211	15.6 (9)	25.5 (16)	0.039 (4)	2.5 (4)	1129	219	332.6 (2)
99	82	/	59132.380298073	6.5 (3)	41.5 (25)	0.027 (2)	1.7 (2)	1088	173	332.3 (3)
100	83	/	59132.380373136	4.6 (3)	42.6 (26)	0.019 (2)	1.2 (2)	1195	228	332.4 (8)
101	84	/	59132.38052385155.0	10.0 (6)	0.054 (6)	3.5 (8)	1229	285	332.7 (0)	
102	85	/	59132.38059868139.0	13.2 (28)	0.051 (5)	3.3 (6)				333.3 (7)
103	86	/	59132.381200771	4.9 (4)	21.4 (13)	0.010 (1)	0.7 (1)	1182	254	332.9 (0)
104	87	/	59132.382139651	5.2 (3)	37.0 (22)	0.019 (2)	1.2 (2)	1098	114	332.8 (1)
105	88	/	59132.38221513519.2	12.0 (20)	0.023 (3)	1.5 (3)	1180	167	332.8 (9)	
106	89	/	59132.382328092	9.3 (10)	6.4 (4)	0.046 (6)	3.0 (7)			332.7 (3)
107	90	/	59132.382590935	2.6 (2)	11.8 (7)	0.024 (3)	1.6 (3)	1156	324	332.6 (2)
108	91	/	59132.382629069	7.1 (7)	19.8 (12)	0.014 (2)	0.9 (2)			331.9 (4)
109	92	/	59132.383567776	4.0 (5)	21.9 (13)	0.009 (1)	0.6 (1)	1342	334	332.7 (1)
110		/	59132.383567810	10.2 (4)	39.4 (24)	0.039 (3)	2.6 (3)	1342	334	332.7 (1)
111	93	/	59132.383719235	6.4 (4)	33.7 (20)	0.021 (2)	1.4 (2)	1365	328	333.1 (2)
112	94	/	59132.384094108	6.0 (2)	17.0 (10)	0.080 (6)	5.2 (8)	1131	243	332.2 (4)
113	95	/	59132.385485123	7.5 (3)	38.4 (23)	0.028 (2)	1.9 (2)	1234	266	332.5 (1)
114	96	/	59132.385748461	2.8 (3)	9.9 (6)	0.022 (4)	1.4 (4)	1277	250	332.7 (7)
115		/	59132.385748500	1.4 (1)	17.1 (10)	0.019 (2)	1.2 (2)	1260	57	332.7 (7)
116	97	/	59132.386613849	6.0 (5)	20.4 (12)	0.012 (2)	0.8 (1)	1215	62	332.6 (6)
117		/	59132.386613911	3.2 (3)	21.3 (13)	0.007 (1)	0.4 (1)	1201	278	332.6 (6)
118		/	59132.386613950	11.1 (12)	13.5 (8)	0.015 (2)	1.0 (2)	1215	62	332.6 (6)
119	98	/	59132.387327364	7.3 (7)	7.3 (4)	0.042 (5)	2.8 (6)	1119	326	333.4 (2)
120		/	59132.387327658	8.3 (7)	21.4 (13)	0.017 (2)	1.1 (2)	1119	326	333.4 (2)
121	99	/	59132.387665472	10.1 (6)	27.4 (17)	0.027 (2)	1.8 (3)	1367	171	332.8 (1)
122		/	59132.38766597730.1	13.9 (8)	0.041 (4)	2.7 (4)				333.4 (3)
123	100	/	59132.387778321	8.1 (6)	23.6 (14)	0.019 (2)	1.2 (2)			332.3 (2)
124	101	/	59132.388681110	6.7 (2)	51.9 (32)	0.034 (2)	2.2 (3)	1320	289	332.8 (2)
125	102	/	59132.390222235	3.4 (3)	30.6 (19)	0.010 (1)	0.7 (1)	1270	112	332.0 (2)
126		/	59132.390222264	8.1 (7)	21.3 (13)	0.017 (2)	1.1 (2)	1498	271	331.8 (2)
127		/	59132.390222596	7.7 (6)	21.0 (13)	0.016 (2)	1.0 (2)	1270	112	333.2 (4)
128	103	/	59132.390447217	5.8 (4)	30.7 (19)	0.018 (2)	1.1 (2)	1299	136	332.6 (0)
129	104	/	59132.390560074	5.8 (4)	29.9 (18)	0.017 (2)	1.1 (2)			332.7 (2)
130	105	/	59132.390973751	9.8 (9)	16.4 (10)	0.016 (2)	1.0 (2)	1301	256	333.3 (5)
131	106	/	59132.391424786	15.2 (9)	24.0 (15)	0.036 (3)	2.3 (3)	1117	297	332.6 (1)
132		/	59132.391424810	7.3 (7)	21.5 (13)	0.015 (2)	1.0 (2)	1117	297	332.6 (1)

**Table 1.** The properties of 563 bursts of SGR 1935+2154 measured with FAST

Pulse ID	Rot. period	T <sub>start</sub> / T <sub>obs</sub>	Pulse ToA <sup>a)</sup>	Width	Peak flux	Fluence	Energy	Cntrl freq.	Bandwidth <sup>b)</sup>	DM <sup>c)</sup>
		(MJD/hour)	(MJD)	(ms)	(mJy)	(Jy ms)	( $\times 10^{27}$ erg)	(MHz)	(MHz)	(pc cm <sup>-3</sup> )
133	107	/	59132.391462366	4.2 (3)	33.6 (20)	0.014 (2)	0.9 (1)	1084	187	333.3 (3)
134		/	59132.391462909	5.3 (5)	21.2 (13)	0.011 (2)	0.7 (1)	1266	293	332.7 (9)
135	108	/	59132.391763134	7.8 (8)	18.1 (11)	0.014 (2)	0.9 (2)	1227	212	332.0 (1)
136	109	/	59132.392402052	4.7 (4)	26.4 (16)	0.012 (2)	0.8 (1)	1061	52	332.5 (1)
137		/	59132.392402304	10.1 (6)	26.0 (16)	0.026 (2)	1.7 (3)	1061	52	332.5 (1)
138	110	/	59132.392739831	26.0 (22)	12.0 (7)	0.031 (3)	2.0 (4)	1299	256	332.8 (2)
139	111	/	59132.393116480	14.0 (8)	23.0 (14)	0.032 (2)	2.1 (3)			332.8 (7)
140	112	/	59132.393417328	1.4 (1)	13.0 (8)	0.015 (2)	0.9 (2)	1270	325	332.1 (4)
141		/	59132.393417380	3.2 (3)	10.3 (6)	0.026 (3)	1.7 (3)			332.1 (4)
142	113	/	59132.394469377	10.6 (11)	15.7 (10)	0.016 (2)	1.1 (2)	1314	281	333.2 (3)
143		/	59132.394469689	15.2 (12)	18.5 (11)	0.028 (3)	1.8 (3)	1213	233	333.1 (4)
144		/	59132.394469967	3.8 (1)	59.4 (36)	0.022 (2)	1.5 (2)	1314	281	332.1 (5)
145	114	/	59132.394846003	1.6 (1)	17.1 (10)	0.022 (2)	1.4 (2)	1127	182	332.0 (7)
146	115	/	59132.395410141	6.1 (5)	22.7 (14)	0.014 (2)	0.9 (1)			333.7 (6)
147	116	/	59132.395785574	6.4 (4)	30.3 (18)	0.019 (2)	1.2 (2)	1133	168	332.0 (6)
148	117	/	59132.395898607	10.3 (8)	20.0 (12)	0.020 (2)	1.3 (2)	1092	48	332.3 (5)
149	118	/	59132.395935550	2.1 (1)	23.8 (14)	0.039 (3)	2.5 (4)	1201	213	333.0 (1)
150	119	/	59132.395973046	4.1 (3)	11.8 (7)	0.038 (4)	2.5 (5)	1080	57	332.7 (3)
151	120	/	59132.396123131	4.5 (2)	41.3 (25)	0.018 (2)	1.2 (2)	1160	127	332.7 (1)
152		/	59132.396123160	6.3 (3)	38.7 (24)	0.024 (2)	1.6 (2)			332.7 (1)
153	121	/	59132.396349692	18.4 (18)	11.9 (7)	0.022 (2)	1.4 (3)	1188	242	333.2 (5)
154		/	59132.396349799	7.2 (4)	29.2 (18)	0.021 (2)	1.3 (2)	1090	111	332.3 (7)
155	122	/	59132.396574951	20.1 (19)	13.1 (8)	0.026 (3)	1.7 (3)	1189	253	332.4 (2)
156		/	59132.396575314	5.7 (4)	26.3 (16)	0.015 (2)	1.0 (1)			332.6 (1)
157	123	/	59132.396838280	10.1 (7)	21.2 (13)	0.021 (2)	1.4 (2)			333.0 (7)
158	124	/	59132.397025524	10.6 (6)	28.0 (17)	0.029 (2)	1.9 (3)	1367	102	332.7 (0)
159		/	59132.397025744	11.5 (2)	73.8 (45)	0.083 (6)	5.4 (7)			332.7 (0)
160		/	59132.397025786	16.9 (5)	42.5 (26)	0.070 (5)	4.6 (6)	1086	47	332.7 (0)
161	125	/	59132.397590450	4.8 (4)	26.3 (16)	0.012 (2)	0.8 (1)			333.6 (6)
162	126	/	59132.397928124	5.3 (3)	36.3 (22)	0.019 (2)	1.2 (2)	1270	212	333.2 (5)
163		/	59132.397928171	18.7 (11)	20.2 (12)	0.037 (3)	2.4 (4)	1270	212	333.0 (6)
164		/	59132.397928204	2.5 (2)	40.4 (25)	0.010 (1)	0.6 (1)	1270	212	333.0 (6)
165	127	/	59132.397965894	5.3 (4)	25.3 (15)	0.013 (2)	0.9 (1)			332.5 (8)
166	128	/	59132.398078455	10.4 (12)	15.0 (9)	0.015 (2)	1.0 (2)			332.6 (2)
167	129	/	59132.398228922	4.7 (5)	23.3 (14)	0.011 (2)	0.7 (1)			332.9 (9)
168	130	/	59132.398342103	11.8 (9)	20.2 (12)	0.023 (2)	1.5 (3)	1258	272	332.9 (2)
169	131	/	59132.399430825	6.4 (5)	8.5 (5)	0.043 (4)	2.8 (5)	1141	183	333.3 (5)
170	132	/	59132.399582480	8.7 (7)	22.2 (13)	0.019 (2)	1.2 (2)	1217	112	333.3 (8)
171	133	/	59132.399920510	11.4 (9)	17.0 (10)	0.019 (2)	1.2 (2)	1158	178	333.2 (5)
172		/	59132.399920766	6.2 (3)	32.3 (20)	0.020 (2)	1.3 (2)	1158	178	332.4 (1)
173	134	/	59132.400070489	5.9 (9)	14.5 (9)	0.008 (2)	0.6 (1)			333.2 (2)
174		/	59132.400070509	5.4 (6)	18.7 (11)	0.010 (2)	0.7 (1)			333.2 (2)
175	135	/	59132.400258701	3.0 (3)	25.8 (16)	0.008 (1)	0.5 (1)	1125	139	332.8 (2)
176	136	/	59132.400296274	10.1 (8)	19.6 (12)	0.020 (2)	1.3 (2)			332.7 (2)
177	137	/	59132.400558890	3.4 (4)	23.3 (14)	0.008 (1)	0.5 (1)	1127	247	333.3 (8)
178		/	59132.400559401	14.8 (13)	17.5 (11)	0.026 (3)	1.7 (3)	1127	247	333.3 (4)

**Table 1.** The properties of 563 bursts of SGR 1935+2154 measured with FAST

Pulse ID	Rot. period	T <sub>start</sub> / T <sub>obs</sub>	Pulse ToA <sup>a)</sup>	Width	Peak flux	Fluence	Energy	Cntrl freq.	Bandwidth <sup>b)</sup>	DM <sup>c)</sup>
		(MJD/hour)	(MJD)	(ms)	(mJy)	(Jy ms)	( $\times 10^{27}$ erg)	(MHz)	(MHz)	(pc cm <sup>-3</sup> )
179	138	/	59132.400746752	15.4 (12)	17.0 (10)	0.026 (2)	1.7 (3)			332.8 (9)
180	139	/	59132.401048117	1.6 (1)	16.9 (10)	0.021 (2)	1.4 (2)	1096	103	332.9 (3)
181	140	/	59132.401235875	17.9 (12)	17.9 (11)	0.031 (3)	2.0 (3)			332.6 (2)
182	141	/	59132.401461345	5.5 (2)	35.2 (21)	0.019 (2)	1.2 (2)	1129	245	332.6 (1)
183		/	59132.401461418	7.5 (7)	17.0 (10)	0.012 (2)	0.8 (1)	1148	209	332.6 (1)
184		/	59132.401461462	20.1 (17)	12.9 (8)	0.025 (3)	1.7 (3)	1105	122	332.6 (1)
185	142	/	59132.401837156	4.3 (3)	29.6 (18)	0.012 (2)	0.8 (1)	1107	92	332.4 (3)
186	143	/	59132.401875155	9.3 (6)	26.0 (16)	0.024 (2)	1.5 (2)	1102	293	332.8 (1)
187	144	/	59132.401912229	9.7 (1)	109.6 (67)	0.104 (6)	6.8 (8)			332.6 (0)
188	145	/	59132.402175757	10.9 (21)	7.4 (4)	0.008 (2)	0.5 (2)	1000	110	332.6 (2)
189		/	59132.402175793	8.8 (8)	20.8 (13)	0.018 (2)	1.2 (2)	1316	161	332.6 (2)
190	146	/	59132.402212999	28.4 (29)	10.5 (6)	0.029 (4)	1.9 (4)	1332	315	332.6 (0)
191	147	/	59132.402288369	10.2 (9)	19.5 (12)	0.019 (2)	1.3 (2)			333.0 (0)
192		/	59132.402288420	13.8 (11)	17.2 (10)	0.023 (2)	1.5 (3)			331.8 (3)
193	148	/	59132.402513934	4.6 (4)	11.7 (7)	0.042 (4)	2.8 (6)	1000	253	332.4 (3)
194	149	/	59132.402551167	6.4 (6)	21.6 (13)	0.014 (2)	0.9 (2)	1443	252	332.7 (9)
195		/	59132.402552126	9.5 (9)	16.6 (10)	0.016 (2)	1.0 (2)	1443	252	332.6 (8)
196	150	/	59132.40270139727.6	(16)	17.4 (11)	0.047 (4)	3.1 (5)			332.5 (4)
197	151	/	59132.402890426	13.8 (12)	8.0 (5)	0.044 (5)	2.9 (6)			333.7 (4)
198	152	/	59132.403378213	3.4 (2)	48.0 (29)	0.016 (2)	1.0 (1)	1303	242	332.2 (4)
199	153	/	59132.404920037	6.4 (3)	35.6 (22)	0.022 (2)	1.5 (2)			333.1 (2)
200		/	59132.404920115	9.9 (9)	17.6 (11)	0.017 (2)	1.1 (2)			333.1 (2)
201		/	59132.404920134	5.5 (6)	20.6 (13)	0.011 (2)	0.7 (1)			333.1 (2)
202	154	/	59132.405408584	11.7 (11)	15.5 (9)	0.018 (2)	1.2 (2)			334.3 (3)
203	155	/	59132.405446146	7.8 (7)	22.6 (14)	0.017 (2)	1.1 (2)	1156	138	332.8 (4)
204		/	59132.405446205	4.7 (3)	29.0 (18)	0.013 (2)	0.9 (1)	1172	175	332.8 (4)
205		/	59132.405446220	3.6 (2)	38.1 (23)	0.013 (2)	0.9 (1)	1188	151	332.8 (4)
206	156	/	59132.405483751	8.8 (6)	23.6 (14)	0.020 (2)	1.3 (2)	1113	224	333.0 (5)
207	157	/	59132.405634259	6.2 (5)	24.9 (15)	0.015 (2)	1.0 (2)	1135	120	332.6 (8)
208	158	/	59132.405746425	19.0 (17)	14.0 (9)	0.026 (3)	1.7 (3)	1311	357	332.8 (3)
209	159	/	59132.406423672	9.1 (6)	26.5 (16)	0.024 (2)	1.6 (2)			333.3 (7)
210	160	/	59132.406498841	9.2 (6)	23.8 (14)	0.022 (2)	1.4 (2)			332.6 (5)
211	161	/	59132.406686893	38.1 (30)	11.1 (7)	0.041 (4)	2.7 (5)			333.3 (4)
212	162	/	59132.407288381	4.3 (3)	33.4 (20)	0.014 (2)	0.9 (1)			332.0 (5)
213	163	/	59132.407438488	4.7 (3)	10.6 (6)	0.039 (4)	2.6 (5)	1357	240	332.8 (2)
214	164	/	59132.407588963	4.5 (3)	38.5 (23)	0.017 (2)	1.1 (2)			333.1 (2)
215	165	/	59132.407626576	12.3 (10)	17.4 (11)	0.021 (2)	1.4 (2)	1191	180	333.0 (2)
216	166	/	59132.407663791	8.9 (6)	24.5 (15)	0.021 (2)	1.4 (2)	1084	63	331.8 (8)
217	167	59133.4096219 / 1.0	59133.409789532	6.8 (6)	18.4 (8)	0.012 (1)	0.8 (1)	1000	145	333.7 (5)
218	168	/	59133.409864449	3.4 (2)	33.5 (14)	0.011 (1)	0.7 (1)			332.8 (4)
219		/	59133.409864482	17.3 (15)	11.6 (5)	0.020 (2)	1.3 (2)			332.8 (4)
220	169	/	59133.410805441	8.1 (6)	6.7 (3)	0.043 (4)	2.8 (4)			332.5 (6)
221	170	/	59133.411819792	4.4 (3)	24.1 (10)	0.011 (1)	0.7 (1)	1199	213	332.2 (8)
222	171	/	59133.412345252	4.8 (4)	20.7 (8)	0.010 (1)	0.6 (1)	1258	175	332.6 (8)
223		/	59133.412345607	2.6 (1)	34.3 (14)	0.009 (1)	0.6 (1)	1277	174	332.6 (8)
224	172	/	59133.412759302	13.5 (7)	19.9 (8)	0.026 (2)	1.7 (2)	1240	271	333.5 (4)

**Table 1.** The properties of 563 bursts of SGR 1935+2154 measured with FAST

Pulse ID	Rot. period	T <sub>start</sub> / T <sub>obs</sub>	Pulse ToA <sup>a)</sup>	Width	Peak flux	Fluence	Energy	Cntrl freq.	Bandwidth <sup>b)</sup>	DM <sup>c)</sup>
		(MJD/hour)	(MJD)	(ms)	(mJy)	(Jy ms)	( $\times 10^{27}$ erg)	(MHz)	(MHz)	(pc cm <sup>-3</sup> )
225		/	59133.412759890	3.8 (4)	22.7 (9)	0.008 (1)	0.6 (1)	1240	271	332.8 (6)
226	173	/	59133.413021817	4.7 (1)	61.9 (25)	0.029 (2)	1.9 (1)	1297	282	332.7 (1)
227	174	/	59133.413059375	3.7 (1)	28.9 (12)	0.084 (4)	5.5 (5)	1248	212	332.6 (0)
228	175	/	59133.413359807	2.5 (1)	36.3 (15)	0.009 (0)	0.6 (0)	1332	191	332.6 (0)
229		/	59133.413359828	5.2 (2)	46.9 (19)	0.024 (2)	1.6 (2)	1266	22	332.6 (0)
230		/	59133.413359854	4.4 (3)	25.4 (10)	0.011 (1)	0.7 (1)	1387	63	332.6 (0)
231	176	/	59133.413397519	2.6 (1)	22.7 (9)	0.047 (3)	3.1 (3)			333.0 (4)
232	177	/	59133.413586495	12.7 (10)	15.2 (6)	0.019 (2)	1.2 (2)	1367	256	333.4 (5)
233	178	/	59133.413661600	7.6 (4)	25.6 (10)	0.019 (2)	1.2 (1)	1281	166	332.4 (2)
234	179	/	59133.413736715	8.2 (6)	19.2 (8)	0.016 (2)	1.0 (1)	1270	185	333.2 (2)
235	180	/	59133.414488414	10.3 (7)	18.7 (8)	0.019 (2)	1.2 (2)			332.5 (3)
236	181	/	59133.415089592	5.3 (1)	90.4 (37)	0.047 (2)	3.1 (2)	1170	325	332.7 (0)
237	182	/	59133.415164923	5.6 (2)	46.9 (19)	0.026 (2)	1.7 (1)	1131	291	332.6 (0)
238	183	/	59133.416819786	9.3 (5)	26.6 (11)	0.024 (2)	1.6 (2)	1354	207	333.6 (1)
239	184	/	59133.417158037	10.6 (8)	15.8 (6)	0.017 (2)	1.1 (1)	1000	185	332.3 (3)
240	185	/	59133.417307702	7.2 (2)	52.1 (21)	0.037 (2)	2.4 (2)			332.6 (1)
241	186	/	59133.418849420	5.3 (4)	26.8 (11)	0.014 (1)	0.9 (1)	1279	205	333.4 (2)
242	187	/	59133.419187946	11.7 (9)	15.3 (6)	0.018 (2)	1.1 (2)	1188	270	332.5 (7)
243	188	/	59133.419487533	3.7 (2)	27.9 (11)	0.010 (1)	0.7 (1)	1320	130	332.4 (3)
244		/	59133.419487554	1.6 (2)	30.2 (12)	0.005 (0)	0.3 (0)	1289	122	332.4 (3)
245	189	/	59133.420089359	8.5 (6)	6.7 (3)	0.045 (4)	2.9 (5)	1205	35	333.2 (3)
246	190	/	59133.420503415	6.2 (5)	23.1 (10)	0.014 (2)	0.9 (1)	1000	110	333.1 (4)
247	191	/	59133.421292318	12.2 (5)	28.7 (12)	0.034 (2)	2.2 (2)	1275	173	332.6 (1)
248	192	/	59133.421518110	6.6 (6)	8.0 (3)	0.041 (4)	2.7 (5)	1221	219	333.3 (2)
249	193	/	59133.421705618	5.9 (1)	59.5 (24)	0.034 (2)	2.2 (2)	1385	302	332.6 (1)
250	194	/	59133.422119056	13.1 (8)	20.2 (8)	0.026 (2)	1.7 (2)	1342	173	332.8 (1)
251		/	59133.422119088	23.9 (16)	14.0 (6)	0.033 (2)	2.1 (3)	1365	62	332.9 (2)
252	195	/	59133.422194053	3.3 (1)	38.9 (16)	0.013 (1)	0.8 (1)	1078	61	332.7 (0)
253		/	59133.422194075	8.5 (1)	69.3 (28)	0.058 (2)	3.8 (3)	1078	61	332.7 (0)
254		/	59133.422194095	6.9 (3)	38.2 (16)	0.026 (2)	1.7 (2)	1078	61	332.7 (0)
255	196	/	59133.422645359	5.4 (5)	22.4 (9)	0.012 (1)	0.8 (1)			332.7 (1)
256		/	59133.422645376	5.3 (5)	21.6 (9)	0.011 (1)	0.7 (1)			332.7 (1)
257		/	59133.422645407	6.8 (4)	33.8 (14)	0.023 (2)	1.5 (2)			332.7 (1)
258	197	/	59133.423134899	5.1 (5)	18.6 (8)	0.009 (1)	0.6 (1)	1232	88	332.7 (8)
259	198	/	59133.423735724	8.4 (5)	23.2 (9)	0.019 (2)	1.2 (1)	1080	77	332.6 (1)
260	199	/	59133.423810759	9.2 (6)	20.4 (8)	0.018 (2)	1.2 (1)	1324	153	332.1 (1)
261	200	/	59133.424224880	9.8 (6)	19.0 (8)	0.018 (2)	1.2 (1)	1240	25	332.9 (7)
262	201	/	59133.424374888	10.1 (7)	18.0 (7)	0.018 (2)	1.2 (1)			332.0 (2)
263	202	/	59133.424524938	13.8 (9)	15.8 (6)	0.021 (2)	1.4 (2)			333.0 (2)
264	203	/	59133.424562488	5.7 (3)	10.7 (4)	0.048 (4)	3.1 (4)	1307	233	332.8 (7)
265	204	/	59133.424750263	5.1 (1)	48.3 (20)	0.024 (2)	1.6 (1)			332.6 (1)
266		/	59133.424750433	5.6 (3)	34.0 (14)	0.019 (2)	1.2 (1)			332.6 (0)
267	205	/	59133.424863464	6.5 (4)	29.8 (12)	0.019 (2)	1.2 (1)	1340	74	332.4 (1)
268		/	59133.424863493	7.9 (6)	21.5 (9)	0.017 (2)	1.1 (1)	1338	73	332.4 (1)
269		/	59133.424863509	4.1 (4)	20.3 (8)	0.008 (1)	0.5 (1)	1346	52	332.4 (1)
270	206	/	59133.425765322	3.6 (1)	45.6 (19)	0.016 (1)	1.0 (1)	1305	314	333.1 (1)

**Table 1.** The properties of 563 bursts of SGR 1935+2154 measured with FAST

Pulse ID	Rot. period	T <sub>start</sub> / T <sub>obs</sub>	Pulse ToA <sup>a)</sup>	Width	Peak flux	Fluence	Energy	Cntrl freq.	Bandwidth <sup>b)</sup>	DM <sup>c)</sup>
		(MJD/hour)	(MJD)	(ms)	(mJy)	(Jy ms)	( $\times 10^{27}$ erg)	(MHz)	(MHz)	(pc cm <sup>-3</sup> )
271		/	59133.425765679	9.9 (6)	20.5 (8)	0.020 (2)	1.3 (2)	1330	126	333.1 (1)
272	207	/	59133.425878615	4.7 (3)	25.6 (10)	0.012 (1)	0.8 (1)	1258	242	333.2 (6)
273	208	/	59133.426254151	5.2 (4)	25.3 (10)	0.013 (1)	0.8 (1)	1088	58	332.6 (3)
274	209	/	59133.426743421	2.5 (2)	16.7 (7)	0.017 (2)	1.1 (2)			332.8 (3)
275	210	/	59133.427119545	3.9 (3)	33.0 (13)	0.013 (1)	0.8 (1)			332.7 (0)
276	211	/	59133.427343853	4.6 (2)	16.8 (7)	0.061 (4)	4.0 (4)	1172	206	332.4 (1)
277	212	/	59133.428546752	5.0 (2)	43.3 (18)	0.021 (1)	1.4 (1)	1332	83	332.5 (1)
278	213	/	59133.428584792	15.2 (7)	23.6 (10)	0.035 (2)	2.3 (2)			332.8 (3)
279	214	/	59133.428998442	9.2 (5)	9.2 (4)	0.067 (5)	4.3 (6)	1305	333	332.7 (2)
280	215	/	59133.429185809	5.0 (4)	11.4 (5)	0.045 (4)	3.0 (5)	1158	253	332.6 (2)
281	216	/	59133.429336097	3.9 (2)	32.0 (13)	0.012 (1)	0.8 (1)	1283	339	331.5 (2)
282	217	/	59133.429636801	4.2 (2)	42.6 (17)	0.018 (1)	1.2 (1)	1301	224	332.7 (1)
283		/	59133.429636855	7.0 (2)	52.1 (21)	0.036 (2)	2.4 (2)	1268	228	332.7 (1)
284	218	/	59133.429674359	4.3 (4)	20.9 (9)	0.009 (1)	0.6 (1)			331.5 (2)
285	219	/	59133.43001314621.2	(20)	9.6 (4)	0.020 (2)	1.3 (2)	1338	262	331.8 (3)
286	220	/	59133.430125968	10.1 (7)	19.2 (8)	0.019 (2)	1.2 (2)	1172	185	332.4 (5)
287	221	/	59133.430201163	8.8 (5)	9.1 (4)	0.063 (4)	4.1 (6)	1289	303	332.4 (7)
288	222	/	59133.430276372	12.8 (12)	12.0 (5)	0.015 (2)	1.0 (2)	1225	253	332.1 (6)
289		/	59133.430276410	6.8 (4)	23.2 (10)	0.016 (1)	1.0 (1)	1318	255	332.1 (6)
290	223	/	59133.430614780	8.3 (3)	40.7 (17)	0.033 (2)	2.2 (2)	1396	199	333.5 (4)
291	224	/	59133.430651817	6.8 (4)	30.0 (12)	0.020 (2)	1.3 (2)	1328	250	331.9 (7)
292		/	59133.430651889	12.5 (7)	21.8 (9)	0.027 (2)	1.8 (2)	1260	298	331.9 (7)
293	225	/	59133.431178029	6.6 (2)	16.3 (7)	0.084 (5)	5.5 (6)	1375	149	332.8 (1)
294	226	/	59133.431215832	4.6 (1)	62.5 (26)	0.029 (2)	1.9 (1)			332.7 (0)
295	227	/	59133.43174238721.5	(22)	9.4 (4)	0.020 (2)	1.3 (2)			332.4 (2)
296	228	/	59133.432117622	30.7 (22)	12.2 (5)	0.037 (3)	2.4 (4)	1129	69	333.0 (1)
297	229	/	59133.432494038	5.3 (2)	17.5 (7)	0.072 (4)	4.7 (5)	1111	103	332.4 (1)
298	230	/	59133.432569129	6.0 (4)	26.2 (11)	0.015 (2)	1.0 (1)			331.5 (3)
299	231	/	59133.432719157	9.7 (8)	16.1 (7)	0.015 (2)	1.0 (1)	1428	106	333.2 (3)
300	232	/	59133.432870110	5.3 (3)	33.6 (14)	0.018 (2)	1.1 (1)			332.8 (2)
301	233	/	59133.432982995	4.0 (1)	74.4 (30)	0.029 (2)	1.9 (2)	1410	122	332.6 (1)
302	234	/	59133.433020448	13.2 (5)	30.0 (12)	0.039 (2)	2.5 (2)			332.8 (1)
303	235	/	59133.433170996	3.8 (1)	47.8 (20)	0.018 (1)	1.2 (1)	1088	78	332.6 (1)
304	236	/	59133.433358609	16.1 (10)	18.9 (8)	0.030 (2)	1.9 (3)	1270	279	332.8 (1)
305	237	/	59133.433470971	7.0 (5)	22.2 (9)	0.015 (2)	1.0 (1)	1311	208	332.8 (9)
306	238	/	59133.433885115	7.3 (3)	33.6 (14)	0.024 (2)	1.6 (1)	1129	155	332.6 (1)
307	239	/	59133.434185859	14.1 (8)	7.3 (3)	0.081 (6)	5.3 (7)			332.9 (4)
308	240	/	59133.434260912	12.4 (7)	21.4 (9)	0.026 (2)	1.7 (2)	1117	57	332.9 (1)
309	241	/	59133.434298681	2.7 (1)	20.1 (8)	0.043 (2)	2.8 (3)	1355	173	333.3 (1)
310	242	/	59133.434335998	5.7 (4)	23.7 (10)	0.013 (1)	0.9 (1)			332.2 (4)
311		/	59133.434336017	6.6 (8)	13.8 (6)	0.009 (1)	0.6 (1)			332.2 (4)
312	243	/	59133.434599457	9.9 (10)	4.8 (2)	0.038 (4)	2.5 (5)	1129	150	333.3 (7)
313	244	/	59133.434937327	13.3 (7)	7.7 (3)	0.080 (6)	5.2 (7)	1277	303	332.5 (8)
314	245	/	59133.435012338	4.5 (3)	26.6 (11)	0.012 (1)	0.8 (1)	1250	242	332.7 (2)
315		/	59133.435012430	7.3 (4)	25.0 (10)	0.018 (2)	1.2 (1)	1250	242	332.7 (2)
316	246	/	59133.435389023	8.1 (4)	27.7 (11)	0.022 (2)	1.4 (2)	1125	265	333.9 (3)

**Table 1.** The properties of 563 bursts of SGR 1935+2154 measured with FAST

Pulse ID	Rot. period	T <sub>start</sub> / T <sub>obs</sub>	Pulse ToA <sup>a)</sup>	Width	Peak flux	Fluence	Energy	Cntrl freq.	Bandwidth <sup>b)</sup>	DM <sup>c)</sup>
		(MJD/hour)	(MJD)	(ms)	(mJy)	(Jy ms)	( $\times 10^{27}$ erg)	(MHz)	(MHz)	(pc cm <sup>-3</sup> )
317	247	/	59133.435463510	2.8 (1)	18.3 (7)	0.041 (3)	2.7 (3)	1123	109	332.8 (2)
318	248	/	59133.435652016	15.7 (9)	19.5 (8)	0.030 (2)	2.0 (2)	1250	225	333.0 (3)
319	249	/	59133.436441083	34.5 (31)	9.2 (4)	0.031 (3)	2.0 (4)	1316	34	332.6 (1)
320	250	/	59133.436628863	5.9 (2)	15.8 (6)	0.073 (4)	4.8 (5)	1146	282	332.6 (1)
321	251	/	59133.436967094	6.5 (5)	25.6 (10)	0.016 (2)	1.1 (1)	1104	94	333.3 (3)
322		/	59133.436968239	7.1 (6)	19.6 (8)	0.014 (2)	0.9 (1)	1104	94	333.4 (3)
323	252	/	59133.437004661	10.7 (2)	52.1 (21)	0.055 (2)	3.6 (3)			332.6 (0)
324	253	/	59133.437042047	4.0 (1)	55.8 (23)	0.022 (1)	1.4 (1)	1348	127	332.6 (1)
325	254	/	59133.437267565	7.6 (3)	15.0 (6)	0.089 (6)	5.8 (7)	1152	201	331.7 (3)
326	255	/	59133.438207576	6.5 (4)	23.6 (10)	0.015 (1)	1.0 (1)	1336	308	333.3 (4)
327		/	59133.438207623	22.5 (21)	10.4 (4)	0.023 (2)	1.5 (3)	1420	237	333.3 (4)
328	256	/	59133.438846797	39.3 (37)	8.8 (4)	0.034 (4)	2.2 (4)	1229	322	332.5 (6)
329	257	/	59133.438922416	13.0 (14)	12.5 (5)	0.016 (2)	1.0 (2)	1105	71	332.4 (8)
330	258	/	59133.439372332	3.5 (3)	29.0 (12)	0.010 (1)	0.6 (1)	1123	52	332.5 (1)
331		/	59133.439372373	1.0 (4)	30.1 (12)	0.025 (12)	1.6 (1)	1422	109	332.5 (1)
332		/	59133.439372522	3.1 (2)	29.4 (12)	0.009 (1)	0.6 (1)	1432	104	332.5 (1)
333	259	/	59133.439523553	11.6 (9)	19.7 (8)	0.022 (2)	1.5 (2)	1385	109	332.9 (0)
334	260	/	59133.439561023	5.9 (3)	11.7 (5)	0.054 (4)	3.5 (5)	1383	178	333.8 (3)
335	261	/	59133.439786661	2.0 (1)	21.2 (9)	0.033 (2)	2.1 (3)	1252	285	333.0 (3)
336	262	/	59133.440425461	4.0 (2)	37.9 (16)	0.015 (1)	1.0 (1)	1137	146	333.5 (4)
337	263	/	59133.441440550	22.9 (17)	14.0 (6)	0.032 (2)	2.1 (3)	1281	274	333.0 (2)
338	264	/	59133.443245149	4.6 (3)	12.1 (5)	0.044 (4)	2.9 (4)	1131	134	332.9 (2)
339	265	/	59133.443432710	4.7 (4)	21.9 (9)	0.010 (1)	0.7 (1)	1168	117	332.9 (2)
340		/	59133.443432742	2.7 (1)	20.7 (9)	0.045 (3)	2.9 (4)	1195	258	332.7 (1)
341	266	/	59133.443922001	3.4 (1)	22.7 (9)	0.060 (4)	3.9 (4)	1209	269	332.5 (1)
342	267	/	59133.444410386	8.7 (5)	29.4 (12)	0.025 (2)	1.6 (2)			332.7 (1)
343	268	/	59133.445049698	8.0 (4)	27.8 (11)	0.022 (2)	1.4 (1)	1336	244	332.7 (7)
344	269	/	59133.446364954	5.2 (3)	29.1 (12)	0.015 (1)	1.0 (1)	1115	75	332.6 (3)
345	270	/	59133.446402379	2.1 (1)	18.1 (7)	0.030 (2)	2.0 (2)	1293	336	332.7 (5)
346	271	/	59133.446552966	5.7 (3)	35.1 (14)	0.020 (2)	1.3 (1)	1119	110	333.0 (2)
347	272	/	59133.446815788	3.3 (2)	15.3 (6)	0.039 (4)	2.6 (4)	1273	317	332.6 (1)
348		/	59133.446816020	6.0 (3)	28.8 (12)	0.017 (2)	1.1 (1)	1307	42	332.6 (1)
349	273	/	59133.447228910	5.5 (3)	28.4 (12)	0.015 (1)	1.0 (1)	1096	128	332.6 (1)
350	274	/	59133.447755503	3.1 (2)	10.2 (4)	0.025 (2)	1.6 (3)	1406	132	333.7 (6)
351	275	/	59133.448507118	4.2 (2)	12.1 (5)	0.040 (3)	2.6 (4)	1166	129	333.4 (2)
352	276	/	59133.448695625	2.9 (2)	11.9 (5)	0.028 (2)	1.8 (3)			332.7 (2)
353	277	/	59133.449259590	9.9 (6)	20.6 (8)	0.020 (2)	1.3 (2)	1123	159	333.7 (5)
354	278	59135.423378 / 1.0	59135.436185470	8.4 (8)	5.7 (2)	0.038 (4)	2.5 (5)	1107	127	332.5 (5)
355	279	/	59135.442914142	7.0 (5)	21.3 (8)	0.015 (2)	1.0 (1)	1107	96	332.8 (5)
356	280	/	59135.450845684	3.8 (2)	14.3 (6)	0.043 (3)	2.8 (3)	1191	270	333.0 (6)
357	281	/	59135.456108457	2.8 (1)	25.9 (10)	0.057 (3)	3.7 (4)	1371	198	332.1 (5)
358	282	/	59135.456183606	14.0 (8)	21.9 (9)	0.030 (2)	2.0 (2)	1113	159	333.3 (4)
359	283	59137.460372 / 1.0	59137.469801943	9.8 (3)	37.6 (16)	0.036 (2)	2.4 (2)	1357	311	332.9 (5)
360	284	/	59137.474200157	11.4 (8)	17.0 (7)	0.019 (2)	1.2 (2)			333.1 (6)
361	285	/	59137.475478193	6.6 (3)	32.6 (14)	0.021 (2)	1.4 (1)	1324	169	332.4 (5)
362	286	/	59137.477771349	5.9 (4)	22.9 (10)	0.013 (1)	0.9 (1)			332.2 (5)

**Table 1.** The properties of 563 bursts of SGR 1935+2154 measured with FAST

Pulse ID	Rot. period	T <sub>start</sub> / T <sub>obs</sub>	Pulse ToA <sup>a)</sup>	Width	Peak flux	Fluence	Energy	Cntrl freq.	Bandwidth <sup>b)</sup>	DM <sup>c)</sup>
		(MJD/hour)	(MJD)	(ms)	(mJy)	(Jy ms)	( $\times 10^{27}$ erg)	(MHz)	(MHz)	(pc cm <sup>-3</sup> )
363	287	/	59137.47901170921.2 (17)	10.8 (5)	0.022 (2)	1.5 (2)	1336	184	332.1 (5)	
364	288	/	59137.4793875962.2 (0)	29.5 (13)	0.052 (3)	3.4 (3)	1088	84	333.6 (3)	
365	289	/	59137.48171821813.7 (10)	14.1 (6)	0.019 (2)	1.2 (2)			332.0 (2)	
366	290	/	59137.48340980513.0 (9)	15.0 (7)	0.019 (2)	1.2 (2)			332.5 (7)	
367	291	/	59137.48525196016.9 (14)	12.4 (6)	0.021 (2)	1.4 (2)	1195	243	332.7 (6)	
368	292	/	59137.4905523249.4 (9)	14.0 (6)	0.013 (2)	0.8 (1)	1221	285	332.4 (5)	
369	293	/	59137.49115355720.4 (11)	19.0 (9)	0.038 (2)	2.5 (3)	1301	255	333.4 (3)	
370	294	59138.4484947 / 1.0	59138.4533635716.6 (7)	14.8 (8)	0.010 (2)	0.6 (1)	1102	139	333.4 (4)	
371	295	/	59138.46986552310.9 (12)	4.4 (2)	0.037 (5)	2.4 (6)	1258	276	332.5 (6)	
372	296	/	59138.47899979610.6 (3)	45.5 (22)	0.047 (3)	3.1 (3)	1312	142	333.4 (4)	
373	297	/	59138.47903739816.5 (10)	22.9 (11)	0.037 (3)	2.4 (3)	1303	217	332.2 (5)	
374		/	59138.4790374214.2 (2)	38.1 (19)	0.016 (2)	1.0 (1)	1301	227	332.2 (5)	
375	298	/	59138.48012764925.1 (21)	11.4 (6)	0.028 (3)	1.8 (3)	1436	380	333.4 (5)	
376	299	/	59138.48666822112.4 (5)	30.1 (16)	0.037 (2)	2.4 (3)	1174	199	331.8 (2)	
377		/	59138.4866688045.9 (5)	22.8 (12)	0.013 (2)	0.9 (1)	1395	250	333.2 (5)	
378	300	59140.3414358 / 5.0	59140.3627486745.5 (3)	35.5 (22)	0.019 (2)	1.2 (2)	1342	260	331.9 (2)	
379	301	/	59140.37925090012.7 (13)	17.4 (11)	0.022 (2)	1.4 (3)	1416	302	333.0 (9)	
380	302	/	59140.3846638606.4 (5)	12.9 (8)	0.065 (6)	4.2 (8)	1350	275	333.0 (2)	
381	303	/	59140.3900767794.4 (3)	14.5 (9)	0.050 (4)	3.3 (6)	1373	173	332.7 (5)	
382	304	/	59140.39056565111.3 (7)	26.4 (16)	0.029 (2)	1.9 (3)			332.8 (1)	
383	305	/	59140.39361041319.8 (13)	20.7 (13)	0.040 (4)	2.6 (4)			332.4 (2)	
384	306	/	59140.3943246565.4 (2)	16.7 (10)	0.071 (6)	4.6 (7)	1365	155	332.2 (7)	
385	307	/	59140.3992488763.4 (2)	43.4 (27)	0.014 (2)	0.9 (1)	1389	165	332.6 (2)	
386	308	/	59140.4001513021.3 (2)	22.2 (14)	0.023 (4)	1.5 (5)	1291	213	332.5 (1)	
387	309	/	59140.40928610910.0 (8)	22.1 (14)	0.022 (2)	1.4 (3)	1283	202	332.3 (3)	
388	310	/	59140.4093231385.9 (5)	25.4 (16)	0.015 (2)	1.0 (2)			332.8 (7)	
389	311	/	59140.4169545573.0 (1)	89.5 (56)	0.027 (2)	1.7 (2)			333.0 (2)	
390	312	/	59140.4228186207.5 (5)	28.2 (18)	0.021 (2)	1.4 (2)	1381	217	333.0 (3)	
391	313	/	59140.4256753165.0 (2)	43.2 (27)	0.021 (2)	1.4 (2)	1225	220	332.8 (2)	
392	314	/	59140.4265402848.7 (8)	11.1 (7)	0.038 (4)	2.5 (5)			333.5 (2)	
393	315	/	59140.4323291963.4 (3)	27.8 (17)	0.009 (1)	0.6 (1)			332.1 (3)	
394	316	/	59140.43319344410.8 (9)	17.0 (11)	0.018 (2)	1.2 (2)	1240	244	333.0 (9)	
395	317	/	59140.43759189210.6 (6)	28.0 (18)	0.029 (2)	1.9 (3)	1344	87	331.9 (7)	
396	318	/	59140.4428167724.8 (4)	29.5 (18)	0.014 (2)	0.9 (2)	1188	204	333.4 (2)	
397	319	/	59140.44375674918.6 (15)	16.7 (10)	0.031 (3)	2.0 (4)	1281	320	332.9 (2)	
398	320	/	59140.44458356710.8 (8)	20.3 (13)	0.021 (2)	1.4 (2)	1248	7	331.4 (2)	
399	321	/	59140.44932008710.4 (10)	20.3 (13)	0.021 (2)	1.4 (3)			331.7 (2)	
400	322	/	59140.4493952929.1 (8)	17.8 (11)	0.016 (2)	1.0 (2)	1166	96	332.6 (2)	
401	323	/	59140.4497338112.2 (1)	45.7 (28)	0.010 (1)	0.6 (1)			331.8 (4)	
402	324	/	59140.4507860485.6 (4)	28.8 (18)	0.016 (2)	1.0 (2)	1193	241	332.7 (1)	
403	325	/	59140.45537216310.0 (9)	18.8 (12)	0.018 (2)	1.2 (2)	1299	290	332.2 (1)	
404	326	/	59140.4666497393.2 (2)	18.5 (11)	0.047 (4)	3.0 (5)	1355	67	332.9 (2)	
405	327	/	59140.4677018794.1 (3)	33.7 (21)	0.014 (2)	0.9 (1)	1279	248	332.8 (2)	
406	328	/	59140.4687170365.8 (3)	31.4 (20)	0.018 (2)	1.2 (2)	1293	288	332.7 (2)	
407	329	/	59140.4739423083.9 (3)	35.9 (22)	0.014 (2)	0.9 (1)	1498	156	332.7 (8)	
408	330	/	59140.4749570385.0 (4)	28.5 (18)	0.014 (2)	0.9 (1)			333.1 (9)	

**Table 1.** The properties of 563 bursts of SGR 1935+2154 measured with FAST

Pulse <i>ID</i>	Rot. period	T <sub>start</sub> / T <sub>obs</sub> (MJD/hour)	Pulse ToA <sup>a)</sup> (MJD)	Width (ms)	Peak flux (mJy)	Fluence (Jy ms)	Energy ( $\times 10^{27}$ erg)	Cntrl freq. (MHz)	Bandwidth <sup>b)</sup> (MHz)	DM <sup>c)</sup> (pc cm <sup>-3</sup> )
409	331	/	59140.479580388	2.1 (1)	27.1 (17)	0.045 (4)	3.0 (4)			333.0 (1)
410	332	/	59140.482701067	5.1 (4)	30.0 (19)	0.015 (2)	1.0 (2)	1215	250	333.6 (3)
411	333	/	59140.483302410	3.7 (2)	44.0 (27)	0.016 (2)	1.0 (1)	1498	201	332.5 (7)
412	334	/	59140.488452461	5.4 (4)	27.6 (17)	0.015 (2)	0.9 (1)			332.5 (8)
413	335	/	59140.48901606540.5	40.5 (41)	9.2 (6)	0.037 (4)	2.4 (5)	1205	239	333.1 (2)
414	336	/	59140.49067003410.8	10.8 (10)	18.4 (12)	0.019 (2)	1.3 (2)			332.6 (7)
415	337	/	59140.500744156	4.6 (3)	33.2 (21)	0.015 (2)	1.0 (2)			331.3 (3)
416	338	/	59140.503601028	3.0 (2)	31.3 (20)	0.009 (1)	0.6 (1)	1232	269	333.0 (2)
417	339	/	59140.510856491	4.8 (4)	32.1 (20)	0.015 (2)	1.0 (2)	1254	309	332.5 (1)
418	340	/	59140.514088989	13.1 (9)	24.7 (15)	0.032 (3)	2.1 (3)	1312	342	333.3 (2)
419	341	/	59140.516570087	5.7 (3)	43.8 (27)	0.025 (2)	1.6 (2)			332.6 (0)
420		/	59140.516570203	9.4 (5)	31.8 (20)	0.029 (2)	1.9 (3)			332.6 (1)
421	342	/	59140.519765215	5.0 (3)	37.7 (24)	0.018 (2)	1.2 (2)	1227	327	331.5 (3)
422	343	/	59140.537057139	5.2 (3)	40.2 (25)	0.020 (2)	1.3 (2)	1193	193	332.7 (7)
423	344	/	59140.546717780	8.1 (8)	19.8 (12)	0.016 (2)	1.0 (2)	1227	177	332.5 (6)
424	345	59143.4678852 / 0.559143.472602196	5.5 (5)	6.8 (3)	0.030 (3)	1.9 (4)	1387	340	333.5 (2)	
425	346	59143.5369889 / 0.559143.539025000	6.6 (4)	25.4 (11)	0.017 (2)	1.1 (1)	1395	45	332.8 (1)	
426	347	/	59143.539100484	8.8 (8)	17.1 (7)	0.015 (2)	1.0 (2)	1242	277	333.6 (3)
427	348	59146.4072689 / 1.059146.408719747	3.4 (3)	7.5 (3)	0.020 (2)	1.3 (2)	1131	120	333.5 (6)	
428	349	/	59146.412592479	1.8 (1)	15.7 (6)	0.022 (2)	1.4 (2)	1236	237	332.3 (2)
429	350	/	59146.414847241	7.6 (5)	20.9 (8)	0.016 (2)	1.0 (1)	1180	166	331.5 (4)
430	351	/	59146.417703629	14.0 (14)	10.7 (4)	0.015 (2)	1.0 (2)	1379	207	333.3 (5)
431	352	/	59146.419358120	4.5 (2)	11.3 (4)	0.040 (3)	2.6 (3)	1318	274	333.0 (2)
432	353	/	59146.419621303	9.4 (7)	16.9 (7)	0.016 (2)	1.0 (1)			333.0 (2)
433	354	/	59146.420748639	1.3 (1)	17.7 (7)	0.018 (2)	1.2 (2)	1266	261	332.8 (2)
434	355	/	59146.420823701	15.9 (10)	17.0 (7)	0.027 (2)	1.7 (2)			332.5 (2)
435	356	/	59146.423793880	5.9 (4)	26.0 (10)	0.015 (1)	1.0 (1)	1285	186	332.9 (2)
436	357	/	59146.437138211	2.7 (3)	32.3 (12)	0.009 (2)	0.6 (1)			332.7 (8)
437	358	/	59146.437213479	15.1 (30)	15.0 (6)	0.022 (4)	1.4 (5)			332.8 (9)
438	359	/	59146.438003547	12.3 (15)	20.2 (8)	0.025 (3)	1.6 (4)			332.6 (2)
439	360	/	59146.441837382	1.5 (0)	44.8 (18)	0.053 (2)	3.5 (3)	1154	257	332.6 (0)
440	361	/	59146.443491247	7.4 (5)	21.4 (8)	0.016 (2)	1.0 (1)			333.0 (7)
441	362	/	59146.446686337	10.3 (5)	28.7 (11)	0.029 (2)	1.9 (2)	1264	196	332.8 (1)
442	363	59147.4902697 / 1.059147.493972814	9.1 (7)	16.1 (8)	0.014 (2)	0.9 (1)	1125	49	331.9 (2)	
443	364	/	59147.495251882	7.5 (2)	20.1 (10)	0.119 (7)	7.7 (9)	1107	106	332.9 (1)
444	365	/	59147.498258514	10.7 (7)	20.6 (10)	0.022 (2)	1.4 (2)	1377	91	332.4 (2)
445	366	/	59147.498748045	5.3 (3)	9.4 (4)	0.040 (4)	2.6 (4)	1117	81	332.6 (2)
446	367	/	59147.508521730	5.0 (4)	25.4 (12)	0.013 (1)	0.8 (1)	1307	292	332.8 (2)
447		/	59147.508521741	2.9 (2)	33.2 (16)	0.009 (1)	0.6 (1)	1326	285	332.8 (2)
448	368	/	59147.512393554	6.4 (4)	27.4 (13)	0.017 (2)	1.1 (2)	1373	110	332.7 (9)
449	369	/	59147.512768518	29.8 (17)	15.9 (8)	0.047 (4)	3.0 (4)	1324	111	332.8 (2)
450	370	/	59147.512843456	1.6 (1)	21.0 (10)	0.026 (2)	1.7 (3)	1113	140	331.9 (2)
451	371	/	59147.518294324	14.3 (13)	15.1 (7)	0.021 (2)	1.4 (2)	1139	88	333.1 (2)
452	372	/	59147.518407474	3.7 (2)	41.1 (20)	0.015 (1)	1.0 (1)	1178	265	333.6 (6)
453	373	59148.4957517 / 1.059148.495925533	3.8 (5)	5.3 (3)	0.016 (2)	1.0 (3)				333.7 (5)
454	374	/	59148.498218515	21.7 (18)	10.7 (7)	0.023 (2)	1.5 (3)	1201	228	332.1 (7)

**Table 1.** The properties of 563 bursts of SGR 1935+2154 measured with FAST

Pulse ID	Rot. period	T <sub>start</sub> /T <sub>obs</sub>	Pulse ToA <sup>a)</sup>	Width	Peak flux	Fluence	Energy	Cntrl freq.	Bandwidth <sup>b)</sup>	DM <sup>c)</sup>
		(MJD/hour)	(MJD)	(ms)	(mJy)	(Jy ms)	( $\times 10^{27}$ erg)	(MHz)	(MHz)	(pc cm <sup>-3</sup> )
455	375	/	59148.499234489	17.8 (11)	17.7 (11)	0.031 (3)	2.0 (3)	1408	210	333.0 (2)
456	376	/	59148.500511462	4.4 (4)	8.8 (6)	0.030 (4)	2.0 (4)	1230	31	333.4 (5)
457	377	/	59148.501114056	2.7 (2)	30.7 (20)	0.008 (1)	0.5 (1)	1234	238	331.9 (5)
458	378	/	59148.501225966	6.1 (3)	10.6 (7)	0.051 (4)	3.3 (5)	1289	252	332.1 (2)
459	379	/	59148.506150247	2.3 (1)	36.9 (23)	0.008 (1)	0.6 (1)			333.0 (0)
460	380	/	59148.506300568	3.3 (4)	19.6 (12)	0.006 (1)	0.4 (1)	1127	179	333.2 (9)
461	381	/	59148.506752208	25.3 (18)	12.7 (8)	0.032 (3)	2.1 (4)	1334	252	332.1 (4)
462	382	/	59148.513179827	2.8 (1)	36.2 (23)	0.010 (1)	0.7 (1)	1342	218	332.7 (2)
463	383	/	59148.514270510	4.7 (4)	27.8 (18)	0.013 (2)	0.8 (1)	1096	94	332.3 (3)
464	384	/	59148.528254299	4.7 (3)	31.7 (20)	0.015 (2)	0.9 (1)			333.4 (3)
465	385	59151.4441591 / 1.0	59151.444200766	15.3 (10)	18.5 (8)	0.028 (2)	1.8 (2)	1111	114	332.6 (1)
466	386	/	59151.444765018	12.1 (6)	8.0 (4)	0.077 (6)	5.0 (7)	1334	246	332.5 (1)
467	387	/	59151.445440888	5.2 (4)	8.2 (4)	0.034 (3)	2.2 (3)	1119	76	333.2 (3)
468	388	/	59151.446042720	2.9 (2)	10.9 (5)	0.025 (2)	1.6 (3)	1137	106	332.3 (1)
469	389	/	59151.446569598	4.6 (1)	23.2 (10)	0.084 (4)	5.5 (5)	1160	132	332.6 (0)
470	390	/	59151.447095236	39.0 (17)	15.6 (7)	0.060 (4)	3.9 (4)			332.4 (1)
471	391	/	59151.447997305	4.2 (4)	8.1 (4)	0.026 (3)	1.7 (3)	1279	225	332.7 (2)
472	392	/	59151.448373629	28.7 (23)	10.4 (5)	0.029 (3)	1.9 (3)	1117	101	333.2 (2)
473	393	/	59151.448486081	2.8 (1)	14.6 (6)	0.032 (2)	2.1 (3)	1281	251	333.0 (1)
474	394	/	59151.448523568	2.7 (1)	15.9 (7)	0.033 (2)	2.2 (3)	1113	106	333.1 (1)
475	395	/	59151.452208232	2.7 (1)	18.6 (8)	0.040 (2)	2.6 (3)	1318	324	332.7 (1)
476	396	/	59151.452396307	7.5 (4)	23.9 (11)	0.018 (2)	1.1 (1)	1150	181	332.7 (1)
477	397	/	59151.452471536	4.9 (3)	21.7 (10)	0.010 (1)	0.7 (1)	1338	301	332.9 (1)
478	398	/	59151.452884390	6.3 (5)	17.7 (8)	0.011 (1)	0.7 (1)	1295	343	332.9 (9)
479	399	/	59151.453372875	7.0 (5)	21.0 (9)	0.015 (2)	0.9 (1)	1262	223	332.4 (2)
480	400	/	59151.455101524	5.4 (4)	21.5 (10)	0.011 (1)	0.7 (1)			332.8 (8)
481	401	/	59151.455516075	13.4 (9)	16.8 (7)	0.022 (2)	1.4 (2)	1186	284	332.2 (2)
482	402	/	59151.455665704	3.7 (2)	11.6 (5)	0.033 (2)	2.2 (3)	1135	139	332.8 (2)
483	403	/	59151.455928594	1.5 (0)	19.7 (9)	0.023 (2)	1.5 (1)	1244	191	332.7 (2)
484	404	/	59151.456192188	3.0 (3)	8.0 (4)	0.019 (2)	1.2 (2)			333.4 (0)
485	405	/	59151.457056926	6.8 (11)	10.9 (5)	0.007 (1)	0.5 (1)	1086	352	332.8 (9)
486	406	/	59151.457996129	3.1 (1)	15.5 (7)	0.037 (2)	2.4 (3)	1312	228	333.6 (1)
487	407	/	59151.458597792	8.3 (3)	34.8 (16)	0.028 (2)	1.9 (2)	1322	173	332.4 (1)
488		/	59151.458597894	20.8 (20)	10.2 (5)	0.021 (2)	1.4 (2)	1369	169	332.4 (1)
489	408	/	59151.458635588	8.7 (5)	9.6 (4)	0.065 (5)	4.3 (6)	1244	165	333.0 (2)
490	409	/	59151.459274371	1.6 (0)	20.8 (9)	0.027 (2)	1.8 (2)	1137	141	333.2 (3)
491	410	/	59151.460064354	15.0 (13)	12.7 (6)	0.019 (2)	1.2 (2)	1312	121	332.5 (4)
492	411	/	59151.460364334	7.8 (6)	17.6 (8)	0.013 (2)	0.9 (1)	1379	212	332.9 (2)
493	412	/	59151.460477763	2.9 (1)	17.1 (8)	0.039 (3)	2.6 (3)	1396	111	332.3 (1)
494	413	/	59151.460514901	1.7 (0)	23.9 (11)	0.032 (2)	2.1 (3)	1117	73	332.4 (1)
495	414	/	59151.460552747	6.9 (6)	6.0 (3)	0.033 (4)	2.1 (4)	1115	109	332.5 (2)
496	415	/	59151.460966314	5.2 (5)	18.1 (8)	0.009 (1)	0.6 (1)			331.6 (4)
497	416	/	59151.461643609	8.8 (6)	19.3 (9)	0.017 (2)	1.1 (1)	1223	257	333.9 (6)
498	417	/	59151.463372722	22.4 (9)	22.4 (10)	0.049 (3)	3.2 (3)	1402	160	333.0 (1)
499	418	/	59151.464499758	11.1 (7)	21.1 (9)	0.023 (2)	1.5 (2)	1293	260	332.7 (1)
500	419	/	59151.464688287	1.6 (0)	28.9 (13)	0.036 (2)	2.3 (2)	1111	94	332.7 (1)

**Table 1.** The properties of 563 bursts of SGR 1935+2154 measured with FAST

Pulse <i>ID</i>	Rot. period	T <sub>start</sub> / T <sub>obs</sub> (MJD/hour)	Pulse ToA <sup>a)</sup> (MJD)	Width (ms)	Peak flux (mJy)	Fluence (Jy ms)	Energy ( $\times 10^{27}$ erg)	Cntrl freq. (MHz)	Bandwidth <sup>b)</sup> (MHz)	DM <sup>c)</sup> (pc cm <sup>-3</sup> )
501	420	/	59151.464988244	4.3 (2)	10.4 (5)	0.035 (3)	2.3 (3)			333.1 (2)
502	421	/	59151.465026211	4.1 (1)	62.4 (28)	0.025 (2)	1.6 (1)	1324	73	332.7 (1)
503	422	/	59151.465063554	20.0 (8)	21.2 (9)	0.042 (2)	2.7 (3)	1133	187	332.6 (1)
504	423	/	59151.465853309	6.9 (5)	22.1 (10)	0.015 (2)	1.0 (1)	1191	191	332.4 (2)
505	424	/	59151.467507027	2.6 (1)	12.4 (6)	0.026 (2)	1.7 (2)	1186	132	333.7 (4)
506	425	/	59151.467957648	1.3 (1)	13.9 (6)	0.015 (2)	1.0 (2)	1086	92	333.0 (1)
507	426	/	59151.468522249	20.1 (16)	11.0 (5)	0.022 (2)	1.4 (2)	1129	84	333.3 (2)
508	427	/	59151.469161239	3.6 (2)	31.7 (14)	0.011 (1)	0.7 (1)	1145	143	332.7 (2)
509		/	59151.469161283	13.6 (9)	17.0 (8)	0.023 (2)	1.5 (2)	1145	143	332.7 (2)
510	428	/	59151.472206315	11.9 (13)	4.4 (2)	0.041 (5)	2.7 (6)			332.4 (6)
511	429	/	59151.472883336	17.3 (14)	4.7 (2)	0.064 (6)	4.2 (8)	1295	133	332.0 (5)
512	430	/	59151.473296879	21.7 (16)	11.8 (5)	0.025 (2)	1.6 (2)	1131	127	333.0 (2)
513	431	/	59151.473484145	6.1 (4)	7.7 (3)	0.037 (4)	2.4 (4)	1152	156	333.1 (2)
514	432	/	59151.475024385	5.7 (3)	29.3 (13)	0.016 (1)	1.1 (1)	1000	255	332.7 (2)
515		/	59151.475024432	15.9 (10)	16.1 (7)	0.025 (2)	1.6 (2)	1000	255	332.7 (2)
516		/	59151.475024464	2.2 (2)	29.0 (13)	0.006 (0)	0.4 (0)	1078	101	332.7 (2)
517	433	/	59151.475589376	2.0 (1)	19.7 (9)	0.031 (2)	2.0 (2)	1137	134	332.5 (1)
518	434	/	59151.475965293	17.8 (13)	12.7 (6)	0.022 (2)	1.4 (2)	1131	125	332.5 (2)
519	435	/	59151.478859770	3.8 (2)	11.6 (5)	0.035 (3)	2.3 (3)	1322	229	333.9 (5)
520	436	/	59151.480325642	2.8 (3)	7.4 (3)	0.016 (2)	1.1 (2)	1264	243	333.3 (1)
521	437	/	59151.480626474	2.2 (1)	20.6 (9)	0.035 (2)	2.3 (3)	1365	181	333.2 (3)
522	438	/	59151.481866335	19.3 (10)	17.7 (8)	0.034 (2)	2.2 (3)	1125	117	333.1 (1)
523	439	/	59151.482694162	6.5 (5)	20.8 (9)	0.013 (1)	0.9 (1)	1168	187	332.7 (1)
524	440	/	59151.483858911	4.2 (2)	13.2 (6)	0.044 (3)	2.9 (3)	1143	121	332.8 (1)
525	441	/	59151.484009362	9.4 (4)	25.0 (11)	0.023 (2)	1.5 (2)	1357	87	333.4 (1)
526	442	/	59151.484761817	23.6 (30)	7.0 (3)	0.016 (2)	1.1 (2)			332.4 (2)
527	443	59152.4527431 /	1.059152.462058585	19.1 (17)	4.7 (2)	0.071 (8)	4.6 (9)	1119	119	332.3 (3)
528	444	/	59152.462735075	10.2 (7)	7.3 (4)	0.059 (5)	3.8 (6)			333.4 (1)
529	445	/	59152.463412124	10.7 (9)	16.2 (8)	0.017 (2)	1.1 (2)			331.9 (2)
530	446	/	59152.464164220	11.9 (8)	19.8 (10)	0.023 (2)	1.5 (2)	1109	90	333.1 (3)
531	447	/	59152.464314991	10.9 (8)	17.7 (9)	0.019 (2)	1.2 (2)	1357	274	333.3 (2)
532	448	/	59152.464802596	13.5 (6)	28.3 (14)	0.037 (2)	2.4 (3)			332.7 (1)
533	449	/	59152.466495024	2.0 (1)	22.3 (11)	0.035 (2)	2.3 (3)	1096	69	333.6 (1)
534	450	/	59152.466945646	16.4 (20)	9.4 (5)	0.015 (2)	1.0 (2)			332.6 (1)
535	451	/	59152.467321687	10.5 (9)	8.8 (4)	0.036 (4)	2.4 (4)			333.1 (4)
536	452	/	59152.467546742	15.8 (12)	14.9 (7)	0.023 (2)	1.5 (2)			332.4 (2)
537	453	/	59152.468787643	23.8 (24)	8.5 (4)	0.020 (2)	1.3 (2)	1232	252	331.9 (6)
538	454	/	59152.469239783	20.4 (11)	18.7 (9)	0.037 (3)	2.4 (3)	1111	110	332.7 (1)
539	455	/	59152.470441535	9.5 (13)	12.2 (6)	0.011 (2)	0.7 (2)	1086	319	332.3 (7)
540	456	/	59152.471457458	4.1 (5)	7.5 (4)	0.024 (3)	1.6 (4)	1170	307	333.3 (1)
541	457	/	59152.471833699	1.9 (0)	30.9 (15)	0.046 (3)	3.0 (4)			332.9 (9)
542	458	/	59152.472960003	5.5 (6)	5.4 (3)	0.023 (3)	1.5 (4)			333.4 (4)
543	459	/	59152.473185535	6.5 (5)	20.7 (10)	0.013 (2)	0.9 (1)	1334	337	332.5 (4)
544		/	59152.473185745	5.4 (2)	39.7 (19)	0.021 (2)	1.4 (1)	1438	294	332.5 (4)
545	460	/	59152.474463527	9.8 (7)	20.0 (10)	0.019 (2)	1.3 (2)	1389	202	333.4 (3)
546	461	/	59152.474690661	2.4 (2)	9.9 (5)	0.018 (2)	1.2 (2)	1268	279	333.4 (3)

**Table 1. The properties of 563 bursts of SGR 1935+2154 measured with FAST**

Pulse <i>ID</i>	Rot. period	T <sub>start</sub> / T <sub>obs</sub> (MJD/hour)	Pulse ToA <sup>a)</sup> (MJD)	Width (ms)	Peak flux (mJy)	Fluence (Jy ms)	Energy ( $\times 10^{27}$ erg)	Cntrl freq. (MHz)	Bandwidth <sup>b)</sup> (MHz)	DM <sup>c)</sup> (pc cm <sup>-3</sup> )
547	462	/	59152.475177870	6.5 (5)	20.9 (10)	0.013 (2)	0.9 (1)	1172	150	332.5 (4)
548	463	/	59152.475628765	8.6 (8)	17.0 (8)	0.014 (2)	0.9 (2)	1000	131	333.1 (2)
549	464	/	59152.477583668	27.1 (25)	9.2 (4)	0.025 (2)	1.6 (3)	1260	247	332.5 (1)
550	465	/	59152.478373979	3.6 (1)	20.5 (10)	0.058 (4)	3.8 (5)	1395	209	332.8 (4)
551	466	/	59152.478712560	10.5 (7)	23.5 (11)	0.024 (2)	1.6 (2)	1244	273	333.4 (8)
552	467	/	59152.481606741	5.8 (4)	8.0 (4)	0.036 (4)	2.4 (4)			332.2 (7)
553	468	/	59152.481907422	8.5 (5)	22.1 (11)	0.018 (2)	1.2 (2)	1248	267	332.9 (2)
554		/	59152.481907458	26.8 (11)	20.8 (10)	0.055 (4)	3.6 (4)	1264	267	332.9 (2)
555	469	/	59152.483485617	4.7 (3)	26.2 (13)	0.012 (1)	0.8 (1)	1123	63	333.2 (4)
556	470	/	59152.484387898	25.3 (14)	16.9 (8)	0.042 (3)	2.7 (4)			332.7 (9)
557	471	/	59152.484689385	14.3 (13)	4.5 (2)	0.051 (6)	3.3 (6)	1266	306	332.9 (2)
558	472	/	59152.487432409	2.1 (2)	11.6 (6)	0.019 (2)	1.2 (2)			332.7 (4)
559	473	/	59152.488711158	4.1 (3)	9.4 (5)	0.030 (3)	2.0 (3)	1135	213	332.2 (7)
560	474	/	59152.490966395	4.9 (4)	23.5 (11)	0.011 (1)	0.7 (1)			331.5 (6)
561	475	/	59152.491078940	2.5 (2)	10.0 (5)	0.019 (2)	1.3 (2)	1131	156	333.1 (9)
562	476	/	59152.491304307	6.9 (5)	18.9 (9)	0.013 (1)	0.8 (1)	1135	152	333.0 (7)
563	477	/	59152.493222036	13.5 (12)	13.6 (7)	0.018 (2)	1.2 (2)	1141	44	333.0 (1)

# Uncertainties in parentheses refer to the last quoted digit.

a) Arrival time of burst peak at the solar system barycenter, after correcting to the infinite frequency.

b) A conservative 30% fractional error is assumed.

c) DM of the pulses obtained from the best burst alignment, calculated using the DM-Power algorithm (<https://github.com/hsiuhsil/DM-power>).

**Table 2.** NICER observations and fitted results

Obs. ID	Obs. time (MJD)	Flux (1.5 keV) ( $10^{-12}$ erg cm $^{-2}$ s $^{-1}$ )	Flux (1.5–2.5 keV) ( $10^{-12}$ erg cm $^{-2}$ s $^{-1}$ )	Flux (2.5–5 keV) ( $10^{-12}$ erg cm $^{-2}$ s $^{-1}$ )	Hardness ratio (keV)	$T_{BB}$	$N_{BB}$	$N_{PL}$	Reduced $\chi^2$ (d.o.f.)
3020560102									
3655010101	58969.06±0.48	4.22±0.07	2.12±0.04	2.10±0.05	0.99±0.03	0.51±0.01	5.66±0.28	2.94±0.48	1.12 (203)
3655010102									
3020560103									
3020560104									
3655010201	58985.10±4.49	3.06±0.06	1.60±0.03	1.46±0.03	0.92±0.03	0.41±0.01	4.03±0.15	3.36±0.28	1.07 (201)
3020560105									
3020560106									
3020560107	58991.04±0.03	2.14±0.07	1.21±0.03	0.93±0.05	0.77±0.04	0.46±0.02	3.45±0.25	1.26±0.5	0.94 (138)
3020560108	58992.01±0.02	3.12±0.10	1.49±0.05	1.63±0.06	1.09±0.05	0.39±0.03	3.29±0.29	4.33±0.6	0.99 (170)
3020560109									
3020560110									
3020560111	58997.34±2.74	2.02±0.06	1.19±0.03	0.83±0.04	0.70±0.04	0.47±0.02	3.64±0.2	0.68±0.37	0.97 (142)
3020560112									
3020560113									
3020560114	59001.11±0.02	2.09±0.09	1.13±0.04	0.95±0.06	0.84±0.06	0.43±0.03	3.01±0.28	1.82±0.55	1.07 (74)
3020560115									
3020560116									
3020560117	59004.60±1.61	1.47±0.06	0.91±0.03	0.56±0.04	0.62±0.05	0.49±0.01	3.01±0.1	-	1.37 (105)
3020560118									
3020560119									
3655010301	59018.13±0.23	1.48±0.05	0.95±0.03	0.53±0.04	0.56±0.04	0.47±0.01	3.17±0.09	-	0.95 (214)
3655010302									
3655010303									
3020560120	59020.72±1.71	1.51±0.05	1.01±0.03	0.51±0.03	0.45±0.01	3.37±0.13	0.05±0.17	0.92 (161)	
3020560121									
3020560122									

**Table 2** continued on next page

**Table 2** (*continued*)

Obs. ID	Obs. time (MJD)	Flux (1.5-5 keV) ( $10^{-12}$ erg cm $^{-2}$ s $^{-1}$ )	Flux (1.5-2.5 keV) ( $10^{-12}$ erg cm $^{-2}$ s $^{-1}$ )	Flux (2.5-5 keV) ( $10^{-12}$ erg cm $^{-2}$ s $^{-1}$ )	Hardness ratio (keV)	$T_{BB}$ (keV)	$N_{BB}$ ( $10^{-5}$ )	$N_{PL}$ ( $10^{-4}$ )	Reduced $\chi^2$ (d.o.f.)
3020560123									
3020560124	59024.50±1.42	1.43±0.05	0.94±0.03	0.50±0.03	0.53±0.04	0.46±0.01	3.13±0.09	-	1.21 (125)
3020560125									
3020560126									
3020560127	59029.14±1.54	1.27±0.05	0.84±0.03	0.43±0.03	0.51±0.04	0.46±0.01	2.83±0.1	-	1.37 (137)
3020560128									
3020560129									
3020560130									
3020560131									
3020560132									
3020560133	59037.18±5.66	1.47±0.05	0.99±0.03	0.48±0.03	0.49±0.04	0.44±0.02	3.32±0.14	0.08±0.18	1.03 (129)
3020560134									
3020560135									
3020560136									
3020560137									
3020560138									
3020560139	59047.34±1.68	1.11±0.05	0.79±0.03	0.32±0.03	0.41±0.04	0.42±0.01	2.76±0.06	-	1.34 (134)
3020560140									
3020560141									
3020560142									
3020560143	59059.64±3.58	1.24±0.07	0.86±0.04	0.38±0.04	0.44±0.06	0.43±0.02	2.97±0.15	-	0.93 (100)
3020560144									
3020560145									
3020560146									
3020560147	59065.97±1.57	1.89±0.06	1.00±0.03	0.89±0.05	0.90±0.05	0.47±0.03	2.63±0.22	1.46±0.42	0.93 (121)
3020560148									
3020560149									
3020560150									
3020560151	59103.56±13.66	1.80±0.06	1.02±0.03	0.79±0.03	0.77±0.04	0.42±0.02	2.84±0.17	1.49±0.31	1.13 (109)

**Table 2** *continued on next page*

**Table 2** (*continued*)

Obs. ID	Obs. time (MJD)	Flux (1.5-keV) (10 <sup>-12</sup> erg cm <sup>-2</sup> s <sup>-1</sup> )	Flux (1.5-2.5 keV) (10 <sup>-12</sup> erg cm <sup>-2</sup> s <sup>-1</sup> )	Flux (2.5-5 keV) (10 <sup>-12</sup> erg cm <sup>-2</sup> s <sup>-1</sup> )	Hardness ratio (keV)	T <sub>BB</sub> (keV)	N <sub>BB</sub>	N <sub>PL</sub>	Reduced $\chi^2$ (d.o.f.)
3020560152									
3020560153									
3655010401	59128.06±0.05	2.16±0.05	1.10±0.02	1.06±0.03	0.96±0.03	0.42±0.02	2.68±0.14	2.4±0.29	0.99 (209)
3655010402	59129.02±0.08	1.31±0.03	0.88±0.02	0.43±0.02	0.49±0.03	0.43±0.02	2.94±0.16	0.15±0.31	0.80 (166)
3020560154									
3020560155									
3020560156	59135.22±3.68	1.42±0.04	0.98±0.03	0.44±0.03	0.45±0.03	0.43±0.01	3.35±0.11	-	1.05 (128)
3020560157									
3020560158									
3020560159									
3020560160	59139.03±0.06	1.44±0.04	0.96±0.02	0.48±0.03	0.50±0.03	0.45±0.01	3.24±0.09	-	0.99 (166)
3020560161	59140.76±0.04	1.05±0.05	0.77±0.03	0.27±0.03	0.35±0.05	0.4±0.02	2.82±0.14	-	1.08 (87)
3020560162	59141.02±0.08	1.55±0.04	0.95±0.02	0.60±0.02	0.63±0.03	0.43±0.02	2.93±0.15	0.74±0.34	0.89 (189)
3020560163	59141.99±0.10	1.33±0.04	0.91±0.02	0.42±0.03	0.46±0.03	0.44±0.01	3.09±0.11	-	1.00 (155)
3020560164	59143.02±0.04	1.56±0.05	0.95±0.03	0.62±0.04	0.65±0.04	0.45±0.03	2.91±0.24	0.61±0.54	0.87 (111)
3020560165	59143.99±0.03	1.60±0.06	0.98±0.03	0.61±0.04	0.62±0.05	0.45±0.02	3.08±0.19	0.46±0.37	1.10 (90)
3020560166	59146.57±0.04	2.31±0.05	1.14±0.03	1.17±0.03	1.03±0.04	0.41±0.02	2.61±0.15	2.83±0.29	1.09 (172)
3020560167	59147.47±0.03	2.56±0.06	1.12±0.03	1.44±0.04	1.29±0.04	0.38±0.03	2.04±0.17	4.1±0.3	1.06 (147)
3020560168	59147.99±0.05	2.32±0.05	1.07±0.02	1.25±0.03	1.16±0.04	0.38±0.02	2.24±0.15	3.43±0.27	0.99 (183)
3020560169	59150.51±0.01	2.30±0.09	1.18±0.05	1.12±0.06	0.95±0.07	0.47±0.03	3.02±0.32	1.95±0.58	1.10 (56)
3020560170	59165.63±0.02	1.59±0.07	1.00±0.04	0.60±0.05	0.60±0.05	0.45±0.02	3.16±0.22	0.42±0.38	1.08 (48)
3020560171	59166.53±0.04	1.38±0.04	0.93±0.03	0.45±0.03	0.49±0.03	0.45±0.01	3.14±0.09	-	0.91 (113)
3020560172	59172.47±0.03	1.33±0.05	0.87±0.03	0.45±0.03	0.52±0.04	0.42±0.02	2.87±0.16	0.34±0.29	0.80 (78)
3020560173	59173.50±0.08	1.81±0.04	1.03±0.02	0.78±0.02	0.76±0.03	0.43±0.01	2.9±0.11	1.36±0.2	1.04 (225)

**Notes.**

(1): ‘-’ means parameter could not be well constrained.

**Table 3.** SWIFT-XRT observations and fitted results

Obs. ID	Obs. time (MJD)	Flux (1.5-keV) ( $10^{-12}$ erg cm $^{-2}$ s $^{-1}$ )	Flux (1.5-2.5 keV) ( $10^{-12}$ erg cm $^{-2}$ s $^{-1}$ )	Flux (2.5-5 keV)	Hardness ratio (keV)	$T_{BB}$	$N_{BB}$	$N_{PL}$	Reduced $\chi^2$ (d.o.f.)
00033349046									
00033349047									
00033349048									
00033349049									
00033349050	58970.75±2.19	3.33±0.14	1.61±0.07	1.72±0.09	1.07±0.07	0.45±0.03	3.60±0.35	3.88±0.43	1.43 (39)
00033349051									
00033349053									
00033349052									
00033349054									
00033349056									
00033349058									
00033349060	58976.15±3.05	2.57±0.12	1.32±0.07	1.25±0.08	0.95±0.08	0.50±0.03	3.54±0.29	1.79±0.33	0.56 (18)
00033349061									
00033349062									
00033349067									
00033349068									
00033349069									
0008904001	59018.51±20.99	1.66±0.08	0.95±0.05	0.71±0.05	0.74±0.06	0.45±0.03	2.75±0.20	1.02±0.23	1.00 (18)
00033349070									
00033349071									
00033349072									
00033349073									
00033349074									
00033349075									
00033349077									
00033349078									
00033349079	59071.79±25.26	1.55±0.08	0.92±0.05	0.63±0.04	0.68±0.06	0.39±0.03	2.80±0.30	1.25±0.27	0.64 (13)

**Table 3** continued on next page

**Table 3** (*continued*)

Obs. ID	Obs. time (MJD)	Flux (1.5-5 keV)	Flux (1.5-2.5 keV)	Flux (2.5-5 keV) ( $10^{-12}$ erg cm $^{-2}$ s $^{-1}$ )	Hardness ratio	$T_{EB}$ (keV)	$N_{BB}$ ( $10^{-5}$ )	$N_{PL}$ ( $10^{-4}$ )	Reduced $\chi^2$ (d.o.f.)
00033349080									
00033349081									
00033349082									
00033349083									
00033349089									
00033349093	59133.62±1.36	1.40±0.14	0.88±0.09	0.52±0.09	0.60±0.12	0.48±0.04	2.91±0.38	0.00±0.37	0.41 (2)
00033349094									
00033349095									

**Notes.**

(1): ‘-’ means parameter could not be well constrained.

## REFERENCES

- Aggarwal, K., Agarwal, D., Lewis, E. F., et al. 2021, ApJ, 922, 115, doi: [10.3847/1538-4357/ac2577](https://doi.org/10.3847/1538-4357/ac2577)
- Anderson, G. E., Gaensler, B. M., Slane, P. O., et al. 2012, ApJ, 751, 53, doi: [10.1088/0004-637X/751/1/53](https://doi.org/10.1088/0004-637X/751/1/53)
- Bailes, M., Bassa, C. G., Bernardi, G., et al. 2021, MNRAS, 503, 5367, doi: [10.1093/mnras/stab749](https://doi.org/10.1093/mnras/stab749)
- Beloborodov, A. M. 2009, ApJ, 703, 1044, doi: [10.1088/0004-637X/703/1/1044](https://doi.org/10.1088/0004-637X/703/1/1044)
- . 2013, ApJ, 777, 114, doi: [10.1088/0004-637X/777/2/114](https://doi.org/10.1088/0004-637X/777/2/114)
- . 2020, ApJ, 896, 142, doi: [10.3847/1538-4357/ab83eb](https://doi.org/10.3847/1538-4357/ab83eb)
- Bera, A., & Chengalur, J. N. 2019, MNRAS, 490, L12, doi: [10.1093/mnrasl/slz140](https://doi.org/10.1093/mnrasl/slz140)
- Bernardini, F., Israel, G. L., Stella, L., et al. 2011, A&A, 529, A19, doi: [10.1051/0004-6361/201016197](https://doi.org/10.1051/0004-6361/201016197)
- Bilous, A. V., Grießmeier, J. M., Pennucci, T., et al. 2022, A&A, 658, A143, doi: [10.1051/0004-6361/202142242](https://doi.org/10.1051/0004-6361/202142242)
- Bochenek, C. D., Ravi, V., Belov, K. V., et al. 2020, Nature, 587, 59, doi: [10.1038/s41586-020-2872-x](https://doi.org/10.1038/s41586-020-2872-x)
- Borghese, A., Coti Zelati, F., Rea, N., et al. 2020, ApJL, 902, L2, doi: [10.3847/2041-8213/aba82a](https://doi.org/10.3847/2041-8213/aba82a)
- Caleb, M., Rajwade, K., Desvignes, G., et al. 2022, MNRAS, 510, 1996, doi: [10.1093/mnras/stab3223](https://doi.org/10.1093/mnras/stab3223)
- Camilo, F., Halpern, J. P., & Ransom, S. M. 2009, The Astronomer's Telegram, 1907, 1
- Camilo, F., Ransom, S. M., Halpern, J. P., et al. 2006, Nature, 442, 892, doi: [10.1038/nature04986](https://doi.org/10.1038/nature04986)
- Camilo, F., Cognard, I., Ransom, S. M., et al. 2007, ApJ, 663, 497, doi: [10.1086/518226](https://doi.org/10.1086/518226)
- Camilo, F., Scholz, P., Serylak, M., et al. 2018, ApJ, 856, 180, doi: [10.3847/1538-4357/aab35a](https://doi.org/10.3847/1538-4357/aab35a)
- CHIME/FRB Collaboration, Andersen, B. C., Bandura, K. M., et al. 2020, Nature, 587, 54, doi: [10.1038/s41586-020-2863-y](https://doi.org/10.1038/s41586-020-2863-y)
- Cordes, J. M., & Chatterjee, S. 2019, ARA&A, 57, 417, doi: [10.1146/annurev-astro-091918-104501](https://doi.org/10.1146/annurev-astro-091918-104501)
- Coti Zelati, F., Rea, N., Pons, J. A., Campana, S., & Esposito, P. 2018, MNRAS, 474, 961, doi: [10.1093/mnras/stx2679](https://doi.org/10.1093/mnras/stx2679)
- González-Caniulef, D., Zane, S., Turolla, R., & Wu, K. 2019, MNRAS, 483, 599, doi: [10.1093/mnras/sty3159](https://doi.org/10.1093/mnras/sty3159)
- Good, D., & Chime/Frb Collaboration. 2020, The Astronomer's Telegram, 14074, 1
- Göğüş, E., Baring, M. G., Kouveliotou, C., et al. 2020, ApJL, 905, L31, doi: [10.3847/2041-8213/abfc8](https://doi.org/10.3847/2041-8213/abfc8)
- Gourdji, K., Michilli, D., Spitler, L. G., et al. 2019, ApJL, 877, L19, doi: [10.3847/2041-8213/ab1f8a](https://doi.org/10.3847/2041-8213/ab1f8a)
- Guver, T., Hu, C.-P., Younes, G., et al. 2021, The Astronomer's Telegram, 14916, 1
- Halpern, J. P., Gotthelf, E. V., Reynolds, J., Ransom, S. M., & Camilo, F. 2008, ApJ, 676, 1178, doi: [10.1086/527293](https://doi.org/10.1086/527293)
- He, K., Zhang, X., Ren, S., & Sun, J. 2016, in Proceedings of the IEEE conference on computer vision and pattern recognition, 770–778
- Hessels, J. W. T., Spitler, L. G., Seymour, A. D., et al. 2019, ApJL, 876, L23, doi: [10.3847/2041-8213/ab13ae](https://doi.org/10.3847/2041-8213/ab13ae)
- Hotan, A. W., van Straten, W., & Manchester, R. N. 2004, PASA, 21, 302, doi: [10.1071/AS04022](https://doi.org/10.1071/AS04022)
- Ilse, M., Tomczak, J., & Welling, M. 2018, in Proceedings of Machine Learning Research, Vol. 80, Proceedings of the 35th International Conference on Machine Learning, ed. J. Dy & A. Krause (PMLR), 2127–2136
- Ioka, K. 2020, ApJL, 904, L15, doi: [10.3847/2041-8213/abc6a3](https://doi.org/10.3847/2041-8213/abc6a3)
- Israel, G. L., Esposito, P., Rea, N., et al. 2016, MNRAS, 457, 3448, doi: [10.1093/mnras/stw008](https://doi.org/10.1093/mnras/stw008)
- Istomin, Y. N., & Sobyanin, D. N. 2007, Astronomy Letters, 33, 660, doi: [10.1134/S1063773707100040](https://doi.org/10.1134/S1063773707100040)
- Jiang, P., Tang, N.-Y., Hou, L.-G., et al. 2020, Research in Astronomy and Astrophysics, 20, 064, doi: [10.1088/1674-4527/20/5/64](https://doi.org/10.1088/1674-4527/20/5/64)
- Karuppusamy, R., Desvignes, G., Kramer, M., et al. 2020, The Astronomer's Telegram, 13553, 1
- Kaspi, V. M., & Beloborodov, A. M. 2017, ARA&A, 55, 261, doi: [10.1146/annurev-astro-081915-023329](https://doi.org/10.1146/annurev-astro-081915-023329)
- Kaspi, V. M., Archibald, R. F., Bhalerao, V., et al. 2014, ApJ, 786, 84, doi: [10.1088/0004-637X/786/2/84](https://doi.org/10.1088/0004-637X/786/2/84)
- Kirsten, F., Snelders, M. P., Jenkins, M., et al. 2021, Nature Astronomy, 5, 414, doi: [10.1038/s41550-020-01246-3](https://doi.org/10.1038/s41550-020-01246-3)
- Kozlova, A. V., Israel, G. L., Svinkin, D. S., et al. 2016, MNRAS, 460, 2008, doi: [10.1093/mnras/stw1109](https://doi.org/10.1093/mnras/stw1109)
- Kramer, M., Stappers, B. W., Jessner, A., Lyne, A. G., & Jordan, C. A. 2007, MNRAS, 377, 107, doi: [10.1111/j.1365-2966.2007.11622.x](https://doi.org/10.1111/j.1365-2966.2007.11622.x)
- Kumar, P., & Bošnjak, Ž. 2020, MNRAS, 494, 2385, doi: [10.1093/mnras/staa774](https://doi.org/10.1093/mnras/staa774)
- Kumar, P., Lu, W., & Bhattacharya, M. 2017, MNRAS, 468, 2726, doi: [10.1093/mnras/stx665](https://doi.org/10.1093/mnras/stx665)
- Levin, L., Bailes, M., Bates, S., et al. 2010, ApJL, 721, L33, doi: [10.1088/2041-8205/721/1/L33](https://doi.org/10.1088/2041-8205/721/1/L33)
- Li, C. K., Lin, L., Xiong, S. L., et al. 2021a, Nature Astronomy, 5, 378, doi: [10.1038/s41550-021-01302-6](https://doi.org/10.1038/s41550-021-01302-6)
- Li, D., Wang, P., Zhu, W. W., et al. 2021b, Nature, 598, 267, doi: [10.1038/s41586-021-03878-5](https://doi.org/10.1038/s41586-021-03878-5)
- Lower, M. E., Younes, G., Scholz, P., et al. 2023, ApJ, 945, 153, doi: [10.3847/1538-4357/acbc7c](https://doi.org/10.3847/1538-4357/acbc7c)

- Lu, W., Kumar, P., & Zhang, B. 2020, MNRAS, 498, 1397, doi: [10.1093/mnras/staa2450](https://doi.org/10.1093/mnras/staa2450)
- Lyne, A., Levin, L., Stappers, B., et al. 2018, The Astronomer's Telegram, 12284, 1
- Lyubarsky, Y. 2014, MNRAS, 442, L9, doi: [10.1093/mnrasl/slu046](https://doi.org/10.1093/mnrasl/slu046)
- Maciesiak, K., & Gil, J. 2011, MNRAS, 417, 1444, doi: [10.1111/j.1365-2966.2011.19359.x](https://doi.org/10.1111/j.1365-2966.2011.19359.x)
- Margalit, B., Beniamini, P., Sridhar, N., & Metzger, B. D. 2020, ApJL, 899, L27, doi: [10.3847/2041-8213/abac57](https://doi.org/10.3847/2041-8213/abac57)
- Mereghetti, S., Savchenko, V., Ferrigno, C., et al. 2020, ApJL, 898, L29, doi: [10.3847/2041-8213/aba2cf](https://doi.org/10.3847/2041-8213/aba2cf)
- Metzger, B. D., Margalit, B., & Sironi, L. 2019, MNRAS, 485, 4091, doi: [10.1093/mnras/stz700](https://doi.org/10.1093/mnras/stz700)
- Niu, C. H., Aggarwal, K., Li, D., et al. 2022, Nature, doi: [10.1038/s41586-022-04755-5](https://doi.org/10.1038/s41586-022-04755-5)
- Olausen, S. A., & Kaspi, V. M. 2014, ApJS, 212, 6, doi: [10.1088/0067-0049/212/1/6](https://doi.org/10.1088/0067-0049/212/1/6)
- Petroff, E., Hessels, J. W. T., & Lorimer, D. R. 2019, A&A Rv, 27, 4, doi: [10.1007/s00159-019-0116-6](https://doi.org/10.1007/s00159-019-0116-6)
- Philippov, A., & Kramer, M. 2022, ARA&A, 60, 495, doi: [10.1146/annurev-astro-052920-112338](https://doi.org/10.1146/annurev-astro-052920-112338)
- Pleunis, Z., Good, D. C., Kaspi, V. M., et al. 2021, ApJ, 923, 1, doi: [10.3847/1538-4357/ac33ac](https://doi.org/10.3847/1538-4357/ac33ac)
- Plotnikov, I., & Sironi, L. 2019, MNRAS, 485, 3816, doi: [10.1093/mnras/stz640](https://doi.org/10.1093/mnras/stz640)
- Ransom, S. M. 2001, in American Astronomical Society Meeting Abstracts, Vol. 199, American Astronomical Society Meeting Abstracts, 119.03
- Rea, N., Pons, J. A., Torres, D. F., & Turolla, R. 2012, ApJL, 748, L12, doi: [10.1088/2041-8205/748/1/L12](https://doi.org/10.1088/2041-8205/748/1/L12)
- Rea, N., Esposito, P., Pons, J. A., et al. 2013, ApJL, 775, L34, doi: [10.1088/2041-8205/775/2/L34](https://doi.org/10.1088/2041-8205/775/2/L34)
- Ridnaia, A., Svinkin, D., Frederiks, D., et al. 2021, Nature Astronomy, 5, 372, doi: [10.1038/s41550-020-01265-0](https://doi.org/10.1038/s41550-020-01265-0)
- Ruderman, M. A., & Sutherland, P. G. 1975, ApJ, 196, 51, doi: [10.1086/153393](https://doi.org/10.1086/153393)
- Salmi, T., Suleimanov, V. F., Näättilä, J., & Poutanen, J. 2020, A&A, 641, A15, doi: [10.1051/0004-6361/202037824](https://doi.org/10.1051/0004-6361/202037824)
- Stamatikos, M., Malesani, D., Page, K. L., & Sakamoto, T. 2014, GRB Coordinates Network, 16520, 1
- Tang, Z., Zhang, S., Dai, S., Li, Y., & Wu, X. 2021, arXiv e-prints, arXiv:2106.04821. <https://arxiv.org/abs/2106.04821>
- Tavani, M., Casentini, C., Ursi, A., et al. 2021, Nature Astronomy, 5, 401, doi: [10.1038/s41550-020-01276-x](https://doi.org/10.1038/s41550-020-01276-x)
- Thompson, C., & Duncan, R. C. 2001, ApJ, 561, 980, doi: [10.1086/323256](https://doi.org/10.1086/323256)
- Thulasiram, P., & Lin, H.-H. 2021, MNRAS, 508, 1947, doi: [10.1093/mnras/stab2692](https://doi.org/10.1093/mnras/stab2692)
- Wang, F. Y., Zhang, G. Q., & Dai, Z. G. 2021, MNRAS, 501, 3155, doi: [10.1093/mnras/staa3912](https://doi.org/10.1093/mnras/staa3912)
- Wang, W., Zhang, B., Chen, X., & Xu, R. 2019, ApJL, 876, L15, doi: [10.3847/2041-8213/ab1aab](https://doi.org/10.3847/2041-8213/ab1aab)
- Wilms, J., Allen, A., & McCray, R. 2000, ApJ, 542, 914, doi: [10.1086/317016](https://doi.org/10.1086/317016)
- Xie, M., Li, Y., Wang, Y., et al. 2022, in Proceedings of the IEEE/CVF Conference on Computer Vision and Pattern Recognition, 7993–8002
- Yang, Y.-P., Zhu, J.-P., Zhang, B., & Wu, X.-F. 2020, ApJL, 901, L13, doi: [10.3847/2041-8213/abb535](https://doi.org/10.3847/2041-8213/abb535)
- Younes, G., Kouveliotou, C., Jaodand, A., et al. 2017, ApJ, 847, 85, doi: [10.3847/1538-4357/aa899a](https://doi.org/10.3847/1538-4357/aa899a)
- Younes, G., Güver, T., Kouveliotou, C., et al. 2020, ApJL, 904, L21, doi: [10.3847/2041-8213/abc94c](https://doi.org/10.3847/2041-8213/abc94c)
- Younes, G., Enoto, T., Hu, C.-P., et al. 2022, The Astronomer's Telegram, 15674, 1
- Zhang, C. F., Jiang, J. C., Men, Y. P., et al. 2020, The Astronomer's Telegram, 13699, 1
- Zhang, Y.-K., Wang, P., Feng, Y., et al. 2022, Research in Astronomy and Astrophysics, 22, 124002, doi: [10.1088/1674-4527/ac98f7](https://doi.org/10.1088/1674-4527/ac98f7)
- Zhou, P., Zhou, X., Chen, Y., et al. 2020, ApJ, 905, 99, doi: [10.3847/1538-4357/abc34a](https://doi.org/10.3847/1538-4357/abc34a)
- Zhu, W., Wang, B., Zhou, D., et al. 2020, The Astronomer's Telegram, 14084, 1
- Zhu, W., Xu, H., Zhou, D., et al. 2023, Science Advances, 9, eadf6198, doi: [10.1126/sciadv.adf6198](https://doi.org/10.1126/sciadv.adf6198)